

Nobeyama 45 m Local Spur CO survey. I. Giant molecular filaments and cluster formation in the Vulpecula OB association

Mikito KOHNO^{1*}, Atsushi NISHIMURA^{2,5,9}, Shinji FUJITA², Kengo TACHIHARA³, Toshikazu ONISHI², Kazuki TOKUDA^{2,4}, Yasuo FUKUI³, Yusuke MIYAMOTO⁴, Shota UEDA², Ryosuke KIRIDOSHI², Daichi TSUTSUMI³, Kazufumi TORII⁵, Tetsuhiro MINAMIDANI^{4,6}, Kazuya SAIGO⁴, Toshihiro HANDA^{7,8} and Hidetoshi SANO⁴

¹Astronomy Section, Nagoya City Science Museum, 2-17-1 Sakae, Naka-ku, Nagoya, Aichi 460-0008, Japan

²Department of Physical Science, Graduate School of Science, Osaka Prefecture University, 1-1 Gakuen-cho, Naka-ku, Sakai, Osaka 599-8531, Japan

³Department of Physics, Graduate School of Science, Nagoya University, Furo-cho, Chikusa-ku, Nagoya, Aichi 464-8602, Japan

⁴National Astronomical Observatory of Japan (NAOJ), National Institutes of Natural Sciences (NINS), 2-21-1 Osawa, Mitaka, Tokyo 181-8588, Japan

⁵Nobeyama Radio Observatory, National Astronomical Observatory of Japan (NAOJ), National Institutes of Natural Sciences (NINS), 462-2, Nobeyama, Minamimaki, Minamisaku, Nagano 384-1305, Japan

⁶Department of Astronomical Science, School of Physical Science, SOKENDAI (The Graduate University for Advanced Studies), 2-21-1, Osawa, Mitaka, Tokyo 181-8588, Japan

⁷Graduate School of Science and Engineering, Kagoshima University, 1-21-35 Korimoto, Kagoshima, Kagoshima 890-0065, Japan

⁸Amanogawa Galaxy Astronomy Research Center (AGARC), Kagoshima University, 1-21-35 Korimoto, Kagoshima, Kagoshima 890-0065, Japan

⁹Institute of Astronomy, The University of Tokyo, 2-21-1, Osawa, Mitaka, Tokyo 181-0015, Japan

*E-mail: kohno@nagoya-p.jp, mikito@a.phys.nagoya-u.ac.jp

Received 2021 February 24; Accepted 2021 October 17

Abstract

We have performed new large-scale ^{12}CO , ^{13}CO , and C^{18}O $J=1-0$ observations toward the Vulpecula OB association ($l \sim 60^\circ$) as part of the Nobeyama 45 m Local Spur CO survey project. Molecular clouds are distributed over ~ 100 pc, with local peaks at the Sh 2-86, Sh 2-87, and Sh 2-88 high-mass star-forming regions in the Vulpecula complex. The molecular gas is associated with the Local Spur, which corresponds to the nearest inter-arm region located between the Local Arm and the Sagittarius Arm. We discovered new giant molecular filaments (GMFs) in Sh 2-86, with a length of ~ 30 pc, width of ~ 5 pc, and molecular mass of $\sim 4 \times 10^4 M_\odot$. We also found that Sh 2-86 contains the three velocity components at 22, 27, and 33 km s^{-1} . These clouds and GMFs are likely to be physically associated with Sh 2-86 because they have high ^{12}CO $J=2-1$ to $J=1-0$ intensity ratios and coincide with the infrared dust

emission. The open cluster NGC 6823 exists at the common intersection of these clouds. We argue that the multiple cloud interaction scenario, including GMFs, can explain cluster formation in the Vulpecula OB association.

Key words: ISM: H II regions — ISM: clouds — ISM: molecules — stars: formation — ISM: individual objects (Vulpecula OB association, Sh 2-86, Sh 2-87, Sh 2-88, NGC 6823, G59.5+0.1, IRAS 19410+2336)

1 Introduction

Giant molecular clouds (GMCs) are the sites of high-mass star and cluster formation (e.g., Lada, & Lada 2003; McKee, & Ostriker 2007). Their formation and evolution processes have been studied in the Milky Way and Local Group Galaxies (e.g., Blitz et al. 2007; Fukui, & Kawamura 2010; Dobbs et al. 2014). Galactic-plane CO surveys by single-dish radio telescopes have revealed the large-scale distribution of GMCs in the Milky Way (e.g., Combes 1991; Heyer, & Dame 2015). The GMCs exist not only in spiral arms but also in inter-arm regions called ‘spurs’, ‘branches’ or ‘bridges’ (e.g., Cohen et al. 1980; Dame et al. 1986). In particular, Ragan et al. (2014) reported that filamentary structures, which they named giant molecular filaments (GMFs) exist in the inter-arm regions of the Milky Way. Long filamentary clouds like GMFs often include the dense molecular gas that forms massive stars and clusters (e.g., Jackson et al. 2010; Wang et al. 2020). Thus, their formation and evolution have been investigated by numerical simulations (e.g., Duarte-Cabral & Dobbs 2017) and observations (e.g., Li et al. 2013; Goodman et al. 2014; Zucker et al. 2015; Wang et al. 2015; Abreu-Vicente et al. 2016; Zhang et al. 2019). Recently, a new spur located between the Local Arm and Sagittarius Arm, has been revealed by parallax measurements of maser spots from the very-long-baseline interferometry (VLBI: Xu et al. 2016) and of OB-type stars from Gaia data (Xu et al. 2018; Xu et al. 2021). In this paper, we refer to this spur structure as a “Local Spur” (see Figure 1 in Reid et al. 2016).

GMCs are essential targets for studying star formation in galaxies, but it is not yet clear what processes are responsible for the formation of massive stars and clusters in inter-arm regions. The Local Spur is the best site for investigating these processes, because it is the inter-arm region nearest to the solar system. In this paper, we present high-resolution CO observations toward the Vulpecula OB association, with the goal of investigating the star-formation processes in a GMC in this inter-arm region in the solar neighborhood. This paper is constructed as follows: Section 2 introduces the Vulpecula OB association, Section 3 presents the datasets, and Section 4 gives the results, including the physical parameters of the molecular clouds. In Section 5, we discuss the NGC 6823 cluster-formation scenario, and in Section 6, we summarize this paper.

2 The Vulpecula OB association in the Local Spur

Table 1. Basic parameters of each H II region in Vulpecula

Name	l [$^{\circ}$]	b [$^{\circ}$]	Luminosity [L_{\odot}]	Earliest Spectral Type	Age	References
Sh 2-86	59.36	−0.18	$\sim 10^{4*}$	O7V ‡	3 ± 1 Myr ‡	[1,2,3]
Sh 2-87	60.88	−0.13	$5.0 \times 10^4*$	B0	3–4 Myr	[4,5, 6]
Sh 2-88	61.47	0.10	$1.3 \times 10^5^{\dagger}$	O8.5V–O9.5V	~ 2 Myr	[4, 6, 7, 8, 9]

[1] Pigulski et al. (2000), [2] Massey et al. (1995), [3] Chapin et al. (2008), [4] Lada, & Lada (2003), [5] Chen et al. (2003), [6] Saito et al. (2007), [7] Deharveng et al. (2000), [8] Marín-Franch et al. (2009), [9] Cappa et al. (2002)

The assumed distances are 2.3 kpc * and 2.0 kpc † . ‡ The values are taken from the cluster in NGC 6823.

The Vulpecula OB association (hereafter Vul OB1) is a high-mass star-forming region, which was first cataloged by Morgan et al. (1953). It is located at $l \sim 60^{\circ}$ in the Galactic plane, and it is a nearby (<3 kpc) massive molecular cloud complex in the Milky Way (see Table 3 in Motte et al. 2018). The Vul OB1 GMC contains the three H II regions: Sh 2-86, Sh 2-87, and Sh 2-88 (Sharpless 1959). Figures 1(a) and 1(b) show three-color composite images obtained with the Herschel space telescope (Pilbratt et al. 2010) as part of the Herschel infrared Galactic Plane Survey (Hi-GAL) project (Molinari et al. 2010a). The $70 \mu\text{m}$ (blue) and $160 \mu\text{m}$ (green) emissions trace the warm dust, whereas the $350 \mu\text{m}$ (red) emission traces the cold dust (e.g., Russeil et al. 2013). Sh 2-86 has diffuse cold dust emission, whereas Sh 2-87 and Sh 2-88 display compact bright emission regions. The basic parameters of these three H II

regions are summarized in Table 1.

2.1 Sh 2-86

Figure 1 (b) shows a close-up image of Sh 2-86 obtained by Herschel (see also Figure 2 in Molinari et al. 2010b and Supplemental Figure 5 in Motte et al. 2018). Sh 2-86 is an H II region that includes the open cluster NGC 6823 (=Cr 405: Collinder 1931), which has been studied by optical observations for more than 60 years (e.g., Barkhatova 1957; Erickson 1971; Turner 1979; Sagar, & Joshi 1981; Stone 1988; Guetter 1992; Shi, & Hu 1999; Olmi et al. 2010; Mottram & Brunt 2012). Massey et al. (1995) identified 17 OB-type stars as members of this open cluster (Table 2). Previous studies have estimated the ages of cluster members to lie within the range 1-5 Myr (Riaz et al. 2012; Pigulski et al. 2000; Kumar et al. 2004). The embedded cluster NGC 6820 (=Cr 404, IRAS 19403+2258: Bica et al. 2008), which corresponds to a compact infrared peak in the Herschel image, is located on the western side of Sh 2-86 at $(l, b) \sim (59^\circ 14, -0^\circ 11)$.

Table 2. Lists of OB-type stars in NGC 6823

Name	Galactic Longitude [degree]	Galactic Latitude [degree]	Spectral Type
	59.50	-0.21	B1 V
	59.51	-0.19	B1.5 III
	59.35	-0.24	B1 V
Erick 93	59.43	-0.16	B1 V
Hoag 8	59.38	-0.18	B1.5 V
Hoag 9	59.43	-0.15	B0.5 V
Hoag 6	59.39	-0.17	B0.5 III
Hoag 2	59.40	-0.15	O7 V((f))
Sharp d	59.41	-0.15	B0.5 V
Sharp e	59.40	-0.15	B0.5 V
HD 344775	59.52	-0.078	B1 III
Sharp n	59.40	-0.14	O9.5Ia
HD 344783	59.37	-0.15	O9.5Ia
Hoag 10	59.38	-0.12	B2 V
Hoag 7	59.41	-0.090	B1.5 V
HD 344776	59.51	0.0015	B0.5 Ia
	59.36	0.016	B1.5 V

References: Massey et al. (1995)

The hyper-compact H II region IRAS 19410+2336 (GAL 059.7+00.1) is found at $(l, b) \sim (59^\circ 78, +0^\circ 06)$ about 15 pc from the cluster NGC 6823 (e.g., Chapin et al. 2008). Energetic outflows and maser sources have been reported in this source (e.g., Szymczak et al. 2000; Beuther et al. 2004; Rodón et al. 2012; Martín-Hernández et al. 2008). Taylor et al. (1992) discovered the supernova remnant (SNR) G59.5+0.1, with a radius of $15'$ and an age of $10^3 - 10^4$ yr (Xu et al. 2005). Xu, & Wang (2012) argued that the G59.5+0.1 progenitor may have induced star formation around the SNR.

2.2 Sh 2-87 and Sh 2-88

Sh 2-87 is a massive star-forming region located at $(l, b) \sim (60^\circ 88, -0^\circ 13)$, and it is composed of compact H II regions. Barsony (1989) reported a molecular outflow from the central embedded source. The Lyman continuum flux derived from observations with the Very Large Array is $1.9 \times 10^{47} \text{ s}^{-1}$, which corresponds to a B0-type exciting star (Barsony 1989).

Sh 2-88 is a compact H II region located at $(l, b) \sim (61^\circ 47, 0^\circ 10)$, and it is excited by an O8.5V-O9.5V star (Deharveng et al. 2000; Cappa et al. 2002). The compact H II regions Sh 2-88A and Sh 2-88B have been studied by optical, infrared, and radio observations since the 1970s as places where compact H II regions interact with molecular clouds (e.g., Lortet-Zuckermann 1974; Pipher et al. 1977; Deharveng, & Maucheraat 1978; Evans et al. 1981).

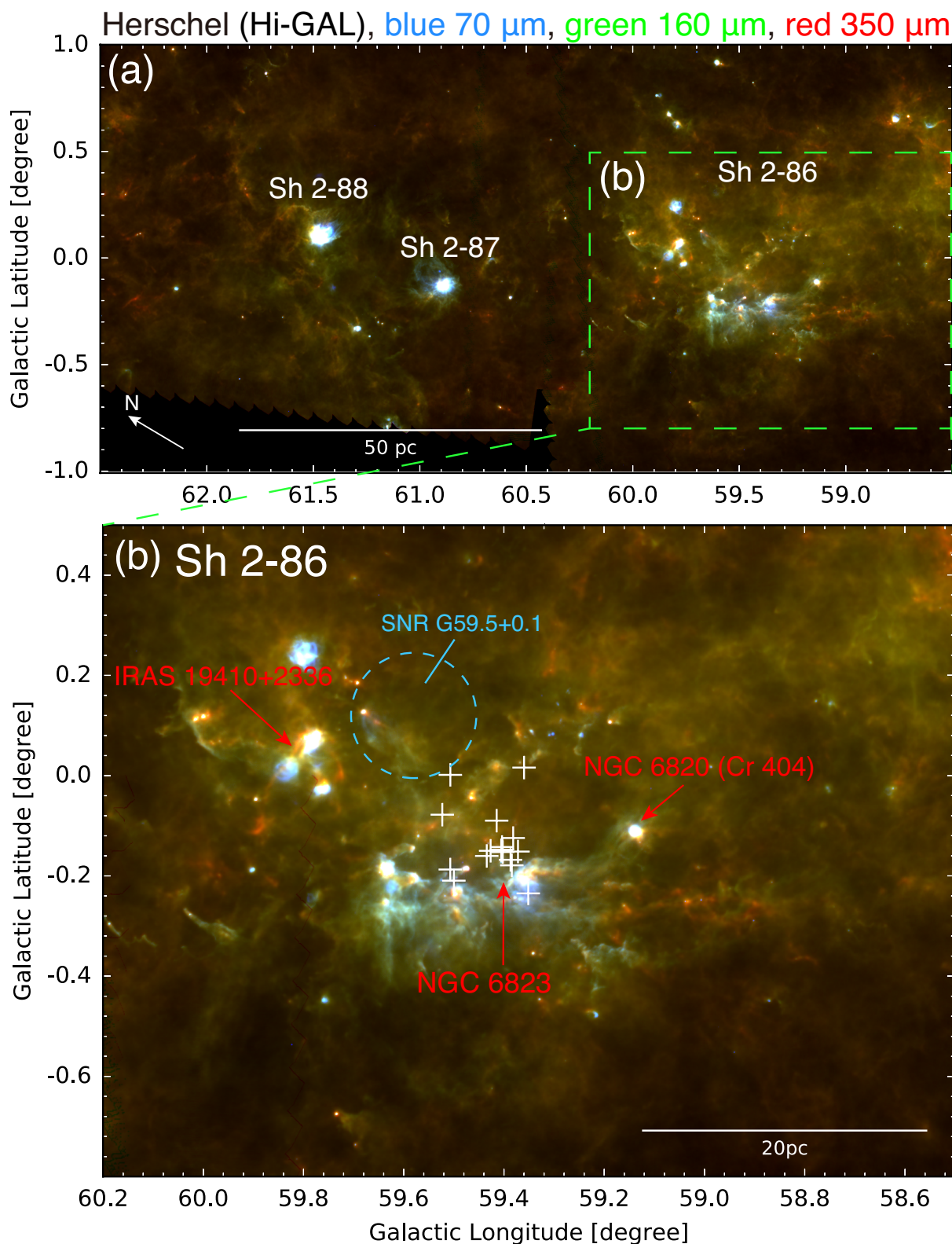


Fig. 1. (a) Herschel three-color composite image of the Vulpecula OB association. Blue, green, and red represent the Herschel/PACS 70 μm , Herschel/PACS 160 μm , and Herschel/SPIRE 350 μm distributions, respectively (Molinari et al. 2016). (b) Close up image of Sh 2-86 (see also Supplemental Figure 5 in Motte et al. 2018). The white crosses indicate the OB-type stars in NGC 6823 identified by Massey et al. (1995). The blue dotted circle shows the position of SNR G59.5+0.1 (Green 2019).

2.3 Star formation scenario and distance to the Vulpecula complex

A propagating star formation scenario has been discussed for Vul OB1 (Turner 1986; Ehlerová et al. 2001) based on Elmegreen, & Lada (1977). On the other hand, Billot et al. (2010) excluded the sequential-star-formation scenario because evolutionary stage of the YSO population is homogeneously distributed in the Vul OB1 GMC. In addition, it has been suggested that the clusters in Sh 2-87 and Sh 2-88 may have originated in star formation triggered by clump-clump collisions (Xue, & Wu 2008; Higuchi et al. 2009; Higuchi et al. 2010).

These previous studies suggest that the H II regions and clusters in the GMC have a common distance of 2.0-2.3 kpc (e.g., Billot et al. 2010). In this paper, we adopt 2.0 kpc, which is the mean of the parallactic distances measured by VLBI to the masers in G059.47-00.18 (1.87 kpc: Xu et al. 2016) and G59.7+0.1 (2.16 kpc: Xu et al. 2009). Figure 2(b) shows the position of Vul OB1 in the Milky Way based on trigonometric parallax measurements (Reid et al. 2019; VERA Collaboration et al. 2020).

The molecular clouds in Vul OB1 were discovered in the 1980s using a 1.2 m radio telescope, but its relationship to star-formation activity was not clear because of the low 8' angular resolution of this study (e.g., Dame, & Thaddeus 1985). Studies of star formation were carried out only in the individual H II regions and open clusters, whereas the entire GMC in Vul OB1 has not yet been studied. Therefore, we performed large-scale high-resolution ($\sim 20''$) CO observations to investigate the relationship of the molecular clouds to star formation in the Vul OB1 GMC.

3 Data sets

Table 3. Observational properties of data sets.

Telescope/Survey	Line	Receiver	HPBW	Effective Resolution	Velocity Resolution	RMS noise [†] level	References
Nobeyama 45-m/ Local Spur	$^{12}\text{CO } J = 1-0$	FOREST	14''	$\sim 20''$	0.5 km s ⁻¹	~ 0.70 K	This work
	$^{13}\text{CO } J = 1-0$	FOREST	15''	$\sim 21''$	0.5 km s ⁻¹	~ 0.30 K	This work
	$\text{C}^{18}\text{O } J = 1-0$	FOREST	15''	$\sim 21''$	0.5 km s ⁻¹	~ 0.30 K	This work
Osaka Pref. 1.85-m/Galactic Plane	$^{12}\text{CO } J = 2-1$		2.7'	$\sim 3.4'$	0.08 km s ⁻¹	~ 0.50 K	[1,2,3]
Telescope/Survey	Band	Detector		Resolution	References		
Herschel/Hi-GAL	70 μm	PACS		$\sim 6''$	[4,5]		
Herschel/Hi-GAL	160 μm	PACS		$\sim 12''$	[4,5]		
Herschel/Hi-GAL	350 μm	SPIRE		$\sim 24''$	[4,6]		

[†] The value of rms noise levels are for the smoothed (in space and velocity) data sets.

References [1] Onishi et al. (2013), [2] Nishimura et al. (2015), [3] Nishimura et al. (2020) [4] Molinari et al. (2016), [5] Poglitsch et al. (2010), [6] Griffin et al. (2010)

3.1 The Nobeyama 45 m Local Spur CO survey project: ^{12}CO , ^{13}CO , and $\text{C}^{18}\text{O } J = 1-0$ observations

We carried out CO $J = 1-0$ observations toward the Vul OB1 GMC from December 2018 to March 2019 using the Nobeyama 45 m telescope. Our data were obtained as part of the Local Spur CO survey (CG181017: PI. A. Nishimura). Figures 2 (a) and 2 (b) show the survey area and a close-up image of Vul OB1 GMC, superposed on a face-on view of the Milky Way. The surveyed area is $l = 50^\circ\text{--}64^\circ$, $b = -1^\circ\text{--}+1^\circ$, and we used the on-the-fly (OTF) scan-mapping mode (Sawada et al. 2008). We observed the Vul OB1 GMC simultaneously in ^{12}CO (115.271 GHz), ^{13}CO (110.201 GHz), and $\text{C}^{18}\text{O } J = 1-0$ (109.782 GHz). This CO survey is an extension of the FUGIN CO Galactic plane survey (Umemoto et al. 2017; Torii et al. 2019; Minamidani et al. 2015; Kohno et al. 2018; Torii et al. 2018; Nishimura et al. 2018; Torii et al. 2021; Fujita et al. 2019; Sofue et al. 2019; Torii et al. 2019; Kohno et al. 2021; Nishimura et al. 2021; Nakanishi et al. 2020). More detailed information will be presented in the project overview paper (Nishimura et al. in preparation). The half-power beam width (HPBW) of the 45 m telescope is 14'' in ^{12}CO and 15'' in ^{13}CO and C^{18}O . The effective beam size convolved with a the Bessel-Gaussian function is 20'' in ^{12}CO and 21'' in ^{13}CO and C^{18}O . The front end was the four-beam, dual-polarization, sideband-separating (2SB) FOur-beam REceiver System on the 45 m Telescope (FOREST: Minamidani et al. 2016; Nakajima et al. 2019). The back-end system was a Spectral Analysis Machine for the 45 m telescope (SAM 45: Kuno et al. 2011), with 4096 channels, which is the same as the ALMA ACA correlator (Kamazaki et al. 2012). The frequency bandwidth and resolution were 31.25 MHz and 15.26 kHz in each window, respectively, using the spectral-window mode¹. We utilized a chopper wheel to convert the raw data to antenna-temperature units (T_a^*) (Ulich, & Haas 1976; Kutner, & Ulich

¹ https://www.nro.nao.ac.jp/~nro45mrt/html/prop/status/Status_latest.html#FOREST_SpW

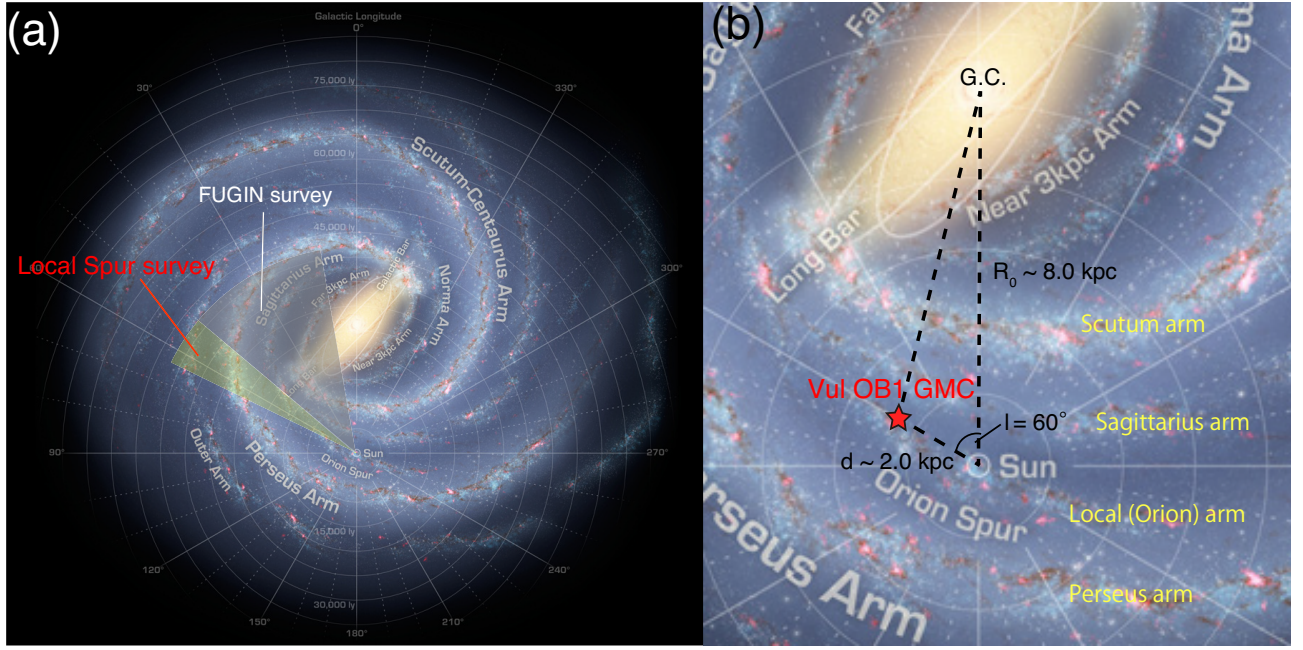


Fig. 2. Top-view of the Milky Way (NASA/JPL-Caltech/ESO/R. Hurt). (a) The gray and yellow shadows show the survey areas of FUGIN and the Local Spur CO survey project, respectively. (b) The star symbol indicates the position of Vul OB1. The distances to the Galactic Center (R_0) and to Vul OB1 (d) are adopted from the VLBI astrometry results: R_0 (~ 8.0 kpc) was obtained by the averaged value of Reid et al. (2019) and VERA Collaboration et al. (2020), and d (~ 2.0 kpc) was obtained by the averaged value of Xu et al. (2009, 2016).

1981). We derived the scaling factor by converting T_a^* to the main beam temperature (T_{mb}) and comparing it with the FUGIN data for the standard source W51A (Fujita et al. 2021a). The pointing accuracy was checked to be within $2''$ - $3''$ by observing the 43 GHz SiO maser source IRAS 19252+2201 (l, b) = ($56^\circ 61', 2^\circ 47'$) every 90 min using the H40 high electron mobility transistor (HEMT) receiver. The data were smoothed using a two-dimensional Gaussian kernel function with the full width at half maximum of $36''$ to achieve the final resolution of $40''$. In this paper, we analyzed the final cube with the grid size of (l, b, v) = ($10'', 10'', 1.0$ km s $^{-1}$). The root-mean-square (r.m.s) noise levels are ~ 0.70 K, ~ 0.30 K, and ~ 0.30 K in ^{12}CO , ^{13}CO , and C ^{18}O , respectively.

3.2 Osaka Prefecture University 1.85-m radio telescope: CO $J=2-1$ Galactic plane survey

We utilized ^{12}CO $J=2-1$ data obtained with the 1.85-m radio telescope installed at the Nobeyama Radio Observatory and operated by Osaka Prefecture University (Onishi et al. 2013; Nishimura et al. 2015; Nishimura et al. 2020). The HPBW is $2'.7$, and the front-end is a 2SB SIS mixer receiver (Hasegawa et al. 2017). The back-end was a digital spectrometer having 16384 channels. The bandwidth and frequency resolutions were 1 GHz and 61 kHz, which correspond to 250 km s $^{-1}$ and 0.08 km s $^{-1}$ in velocity space, respectively. The calibration was performed by observing Orion KL as a standard source (Nishimura et al. 2015)². The uncertainty in the data is $\sim 10\%$. More detailed information about the 1.85-m radio telescope is provided by Onishi et al. (2013) and Nishimura et al. (2020). The effective resolution of the cube data is $\sim 3'.4$. We analyzed the final 3D cube having a voxel resolution of (l, b, v) = ($60'', 60'', 0.079$ km s $^{-1}$).

3.3 The Hi-GAL project: Herschel far-infrared archival data for the Galactic plane

We also utilized the dust-continuum data obtained from the Herschel Space Observatory (Pilbratt et al. 2010). The public DR1 fits data were taken from the VIALACTEA web page³, which is part of Hi-GAL survey project (Molinari et al. 2010a; Molinari et al. 2010b; Molinari et al. 2016). The far-infrared 70 and 160 μm images were obtained with the Photodetector Array Camera and Spectrometer (PACS). The 350 μm data were obtained with the Spectral and Photometric Imaging REceiver (SPIRE; Griffin et al. 2010). We summarize the basic parameters of the datasets in Table 3.

² <http://www.astro.s.osakafu-u.ac.jp/~nishimura/Orion/>

³ <http://vialactea.iaps.inaf.it/vialactea/eng/index.php>

4 Results

4.1 Large-scale CO velocity distributions in the Local Spur

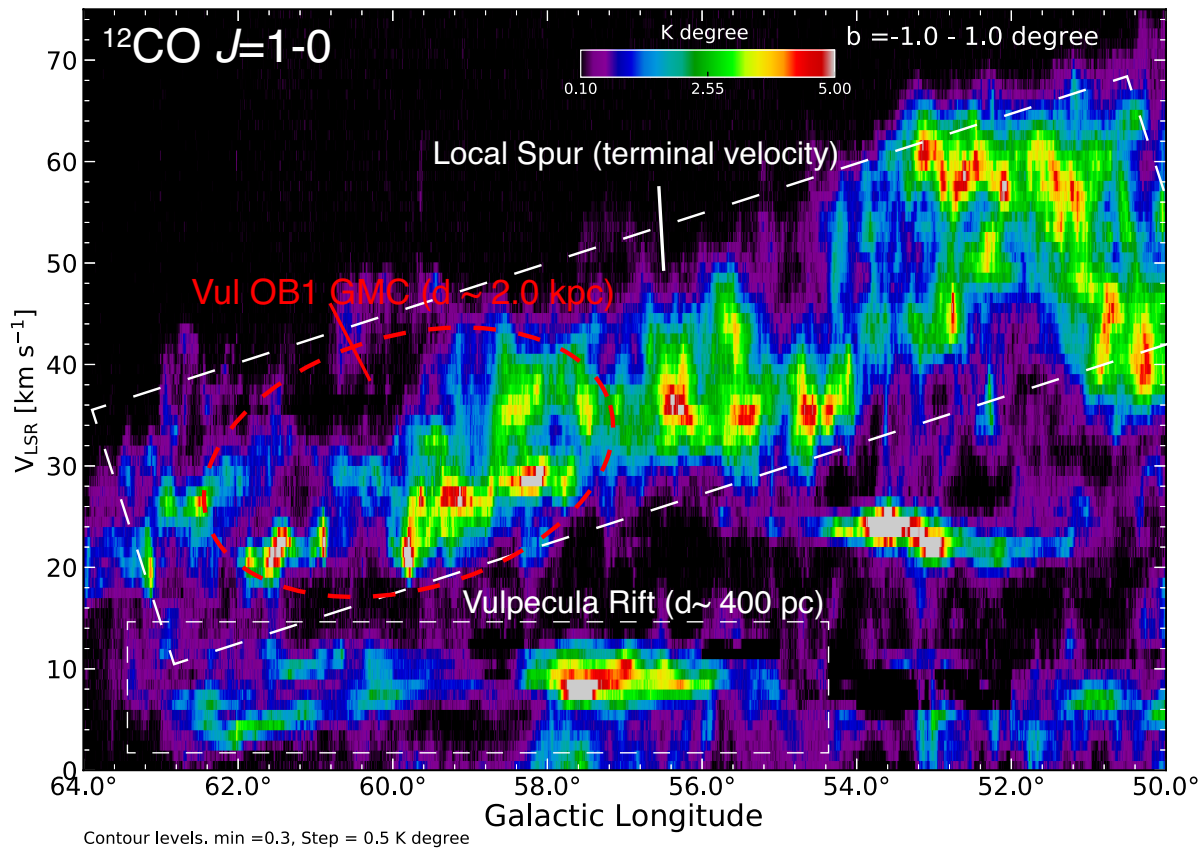


Fig. 3. The large-scale $^{12}\text{CO } J=1-0$ longitude-velocity diagram obtained with the Nobeyama 45 m telescope. White dotted rectangles in the velocity ranges $0-+15 \text{ km s}^{-1}$ and $15-70 \text{ km s}^{-1}$ show the Vulpecula Rift and Local Spur, respectively. The red dotted circle indicates the Vul OB1 GMC.

Figure 3 shows the ^{12}CO longitude-velocity diagram for the entire survey area. We find mainly two components in the velocity range $0-+15 \text{ km s}^{-1}$ and $15-70 \text{ km s}^{-1}$ in this longitude range. The former is the Vulpecula Rift, which contains local clouds in the solar neighborhood with distances of $\sim 400 \text{ pc}$ (e.g., Dame, & Thaddeus 1985; Dame et al. 1987). The latter, which is distributed diagonally in the longitude-velocity diagram, is the Local Spur, which corresponds to the inter-arm region between the Local Arm and Sagittarius Arm (Reid et al. 2016; Xu et al. 2016). This velocity range also corresponds to the terminal velocity in the first quadrant of the Galaxy (e.g., Burton & Gordon 1978; McClure-Griffiths, & Dickey 2016). The GMC associated with Vul OB1 is part of the Local Spur in the velocity range $15-40 \text{ km s}^{-1}$. We also point out another velocity cloud around $(l, v) \sim (53^\circ, 23 \text{ km s}^{-1})$. This cloud corresponds to GMF 54.0-52.0 (Ragan et al. 2014). GMF 54.0-52.0 includes dense gas (Wang et al. 2020) and shows signatures of massive star formation in the N115 infrared bubble reported by previous studies (Xu & Ju 2014; Zychová & Ehlerová 2016). A detailed analysis of this cloud will be presented in a separate paper.

4.2 CO spatial distributions in Vul OB1

Figure 4 presents the integrated intensity maps of (a) ^{12}CO , (b) ^{13}CO , and (c) C^{18}O . The molecular clouds have peaks in the three H II regions. The intensity peaks in Sh 2-86 correspond to IRAS 19410+2336 and NGC 6823. Sh 2-87 and Sh 2-88 have peaks in the centers of the H II regions. The ^{13}CO molecular gas is distributed within dense regions of ^{12}CO . The C^{18}O emission is hardly detected in the Vul OB1 GMC, and it is localized to a small area within ~ 1 pc from Sh 2-86, Sh 2-87, and Sh 2-88. In this paper, we have carried out more detailed analyses toward Sh 2-86, where the molecular gas is distributed over ~ 30 pc.

Figure 5 shows ^{12}CO velocity channel maps of Sh 2-86. We find a filamentary cloud (Filament A) that is elongated from east to west in the velocity range $21.5\text{--}25.5\text{ km s}^{-1}$, and the CO peaks correspond to the infrared source IRAS 19410+2336. In the velocity range $23.5\text{--}26.5\text{ km s}^{-1}$, we discovered a filamentary cloud (Filament B) that extends over ~ 40 pc from north to south. We also find a filamentary cloud (Filament C) in the velocity range $26.5\text{--}29.5\text{ km s}^{-1}$. Filament C has a length of ~ 30 pc, and it is extended in the direction of Galactic longitude. The CO peaks correspond to NGC 6823 and to the embedded cluster NGC 6820. We point out that Filament B and C are likely to be comparable to the GMFs in the Milky Way reported by Ragan et al. (2014).

On the other hand, there is also a round-shaped cloud in the velocity range $31.5\text{--}34.5\text{ km s}^{-1}$ that is distributed over ~ 10 pc around the cluster NGC 6823. We also present ^{13}CO and C^{18}O velocity channel maps of Sh 2-86 in the Appendix (see Figures 11 and 12).

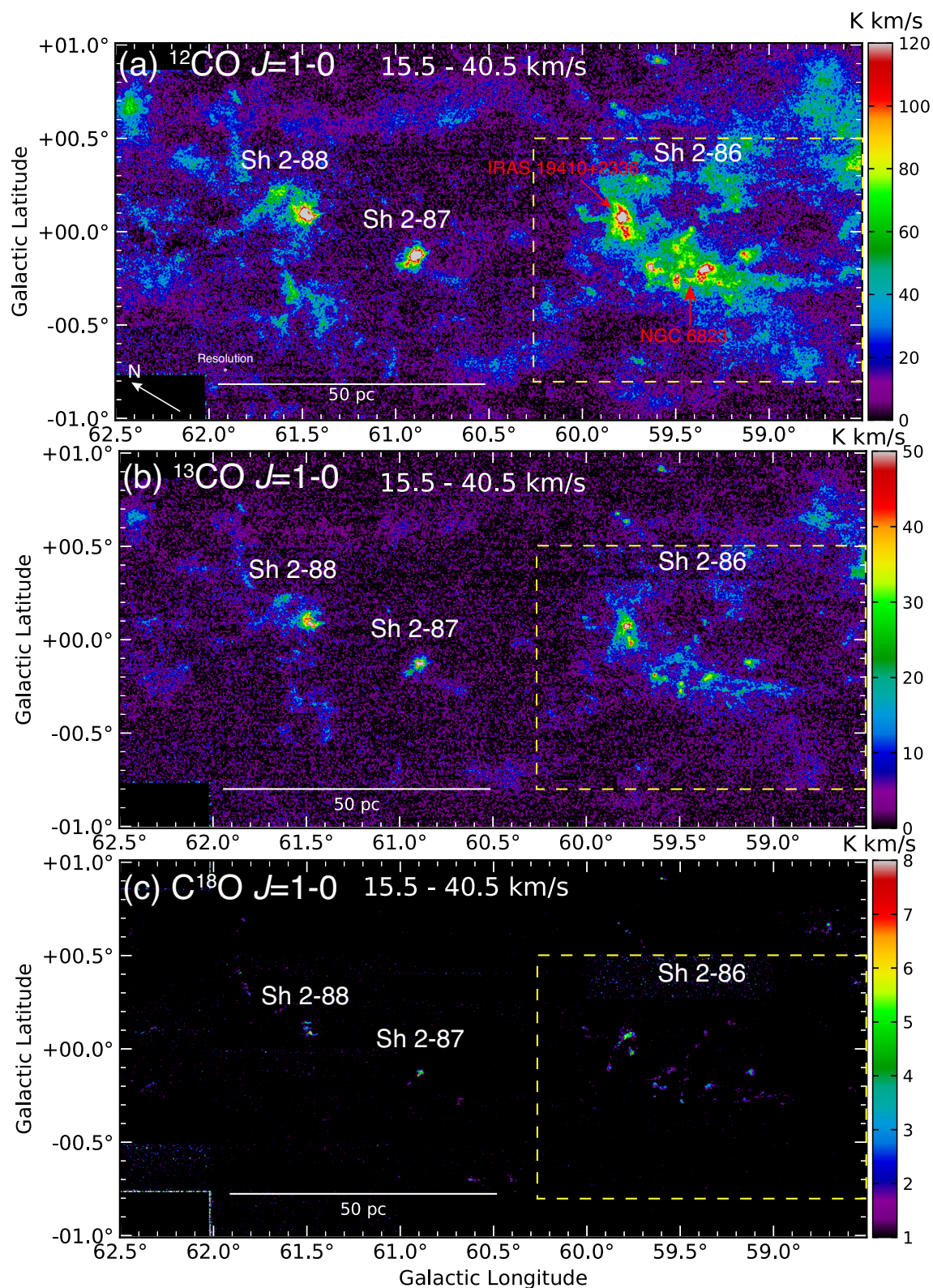
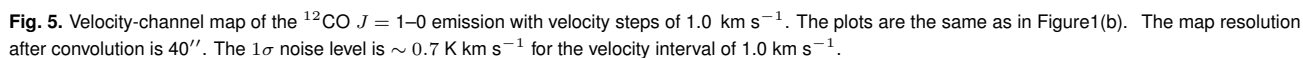


Fig. 4. Integrated intensity maps of (a) ^{12}CO , (b) ^{13}CO , and (c) $\text{C}^{18}\text{O } J=1-0$ for Vul OB1. The yellow dotted boxes show the area presented in the velocity-channel maps in Figure 5. The map resolution after convolution is 40". Pixels of the C^{18}O map are blanked if the line intensity is less than 1.0 K.





4.3 CO velocity distributions and the three velocity components in Sh 2-86

Figure 6 presents the ^{12}CO (a) intensity-weighted velocity map (first-moment) and (b) velocity dispersion (second-moment) maps. We calculated the intensity-weighted velocity (V_c) and velocity dispersion (ΔV) given by

$$V_c = \frac{\int T_B(v) v dv}{\int T_B(v) dv} [\text{km s}^{-1}], \quad (1)$$

$$\Delta V = \left\{ \frac{\int T_B(v) (v - V_c)^2 dv}{\int T_B(v) dv} \right\}^{1/2} [\text{km s}^{-1}] \quad (2)$$

, where $T_B(v)$ and v are the brightness temperature and radial velocity, respectively. The velocity field (Figure 6a) extends $\sim 20 \text{ km s}^{-1}$ around IRAS 19410+2336, and $\sim 28 \text{ km s}^{-1}$ near the cluster NGC 6823. A large velocity dispersion of $\sim 5 \text{ km s}^{-1}$ (Figure 6b) exists at the open cluster NGC 6823, which also corresponds to the intersection of Filament B and Filament C.

Figure 6 (c), (d) show the CO spectra near the NGC 6823 cluster at the position A and B. We find the three velocity components at 22, 27, and 33 km s^{-1} . Blue, green, and red shadow area indicate the integrated velocity range of each component in this paper. We performed a detailed analysis of these multiple velocity components with the goal of determining the relationship between these molecular filaments and cluster formation in Sh 2-86.

4.4 $^{12}\text{CO } J=2-1/1-0$ intensity ratio and comparison to the Herschel dust-continuum images

We performed detailed analyses of the $^{12}\text{CO } J=2-1/1-0$ intensity ratio (hereafter $R_{2-1/1-0}$) and compared it with the infrared image toward these velocity components. Figures 7(a), (b), and (c) show the $R_{2-1/1-0}$ maps of the 22, 27, and 33 km s^{-1} components, respectively. The $^{12}\text{CO } J=1-0$ data were smoothed to $3''.4$, which corresponds to the effective resolution of the $^{12}\text{CO } J=2-1$ data. Pixels are blanked if the integrated intensity is less than 5 K km s^{-1} ($\sim 5\sigma$) for each integrated velocity range. The intensity ratio of the different CO rotational levels is useful for investigating the excitation states of the molecular clouds. The 22 km s^{-1} components has a high-intensity ratio ($R_{2-1/1-0} \sim 0.8 - 1.0$) at NGC 6820 and on the eastern side of IRAS 19410+2336. The 27 km s^{-1} components has a high ratio ($R_{2-1/1-0} \sim 0.9 - 1.0$) at NGC 6823 and NGC 6820. The 33 km s^{-1} components has $R_{2-1/1-0} \sim 0.9 - 1.0$ around NGC 6823. These values are higher than the typical value of $R_{2-1/1-0} \sim 0.6$ in the Galactic plane (e.g., Yoda et al. 2010) and in external spiral galaxies (e.g., Yajima et al. 2021). The value of $R_{2-1/1-0}$ depends on the kinematic temperature of the molecular gas and the number density of hydrogen molecules, assuming the large-velocity-gradient model (e.g., Goldreich & Kwan 1974). Therefore, a high-intensity ratio indicates the presence of dense or warm gas associated with massive stars in these molecular clouds. Figures 7(d), (e), and (f) show the spatial distributions of the three clouds (contours) superposed on the Herschel 160 μm image. We find that the CO peaks in each velocity component correspond morphologically to the infrared peaks of IRAS 19410+2336, NGC 6823, and NGC 6820. From these results, we suggest that these three components, which have the velocity separations of $5\text{--}6 \text{ km s}^{-1}$ are likely to be physically associated with Sh 2-86.

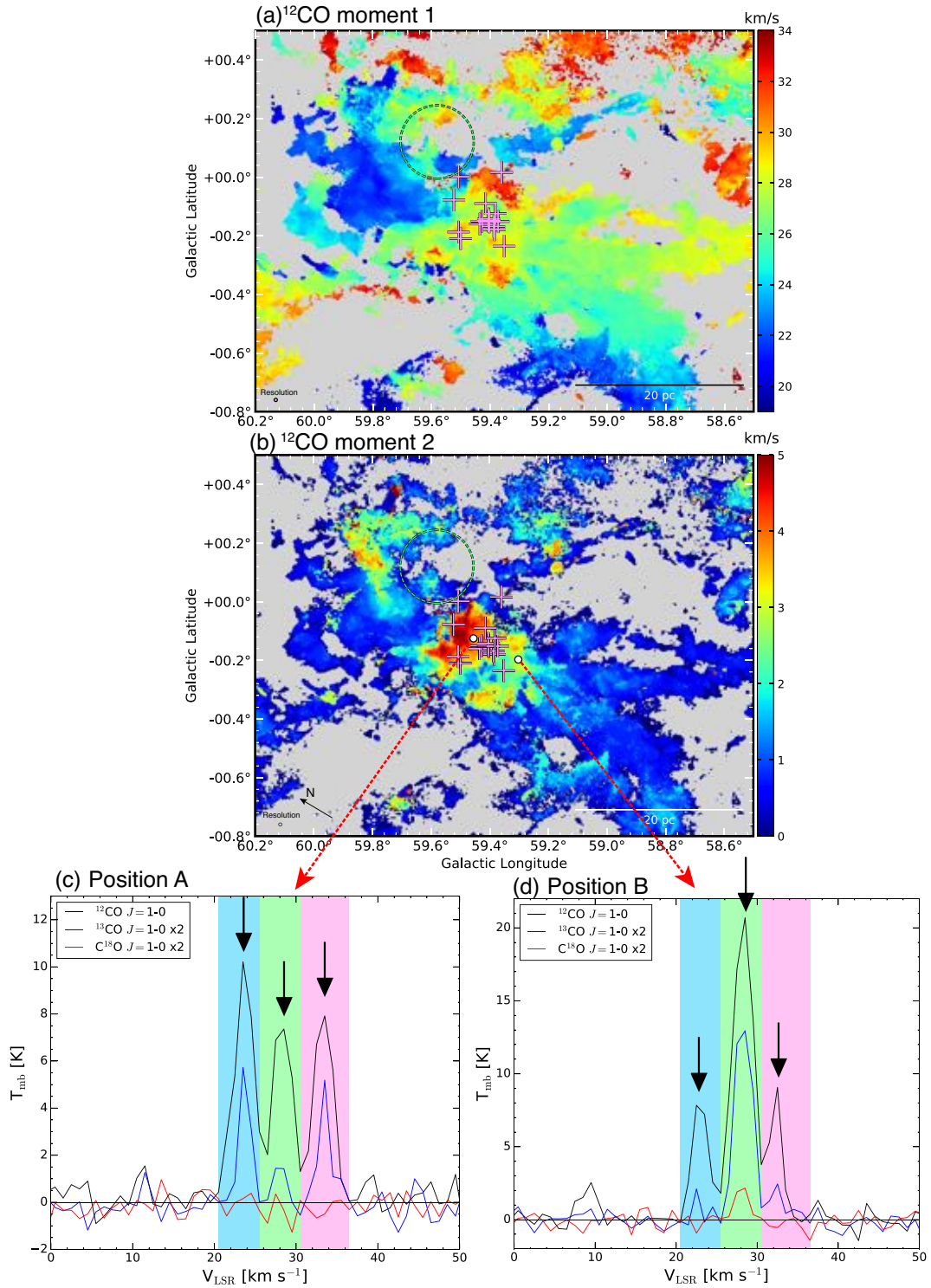


Fig. 6. (a) The ^{12}CO first-moment (velocity-field) map for Sh 2-86. (b) The ^{12}CO second-moment (velocity dispersion) map. The adopted velocity range extends from 19 to 34 km s $^{-1}$. The crosses and dotted circles are the same as in Figure 1(b). Pixels are blanked if the line intensity is less than 3.5 K ($\sim 5\sigma$). The map resolution after convolution is 40''. (c) and (d) The CO spectra observed at two positions indicated by the white circles in panel. Short black arrows show the three velocity components at 22, 27, and 33 km s $^{-1}$. Blue, green, and red shadows show the integrated velocity range of each velocity component in this paper.

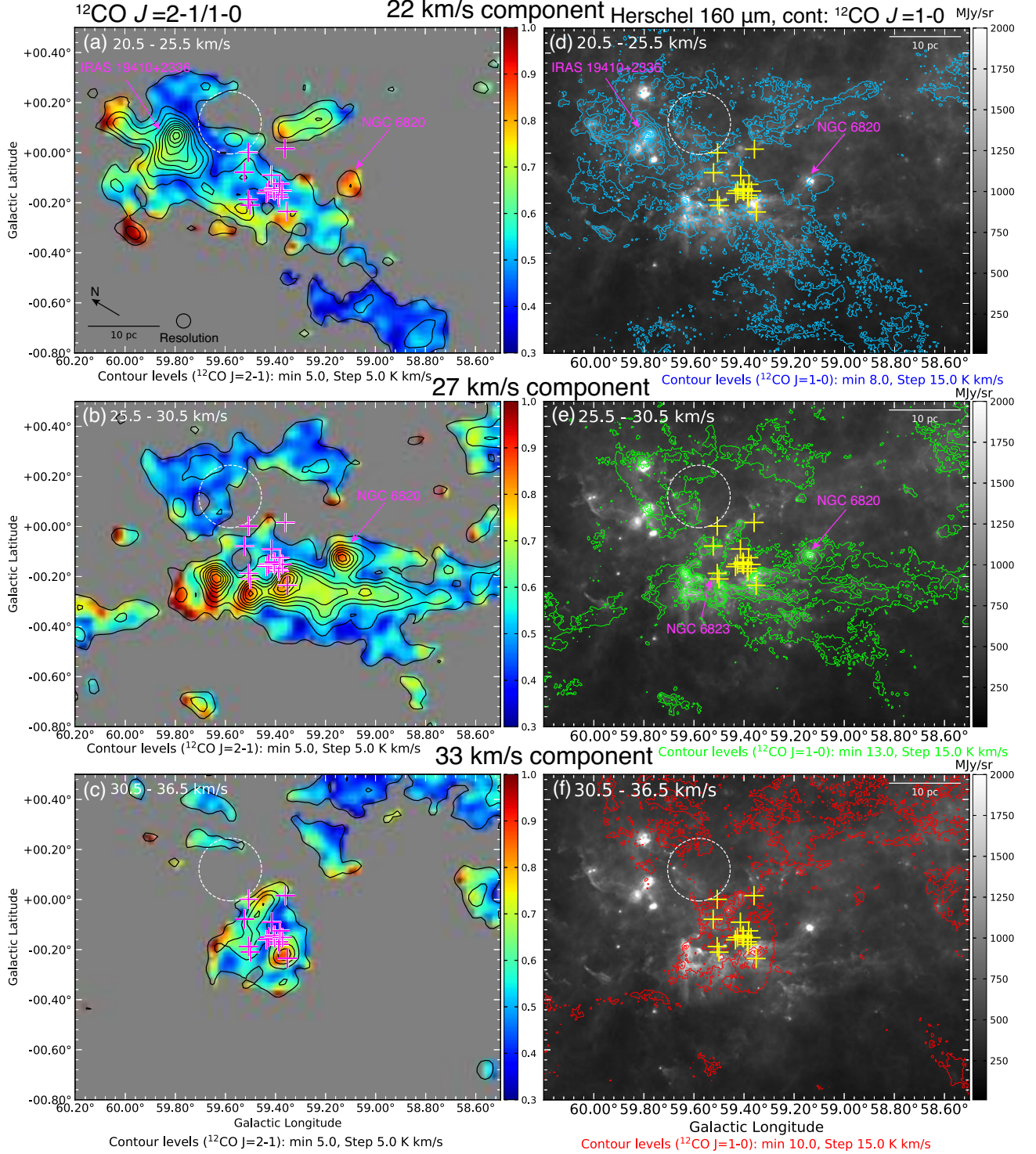


Fig. 7. The $^{12}\text{CO } J=2-1/1-0$ intensity ratios of the (a) 22 km s⁻¹, (b) 27 km s⁻¹, and (c) 33 km s⁻¹ components in Sh 2-86. The map resolution after convolution is 3'.4, which corresponds to the effective resolution of the $^{12}\text{CO } J=2-1$ data. Pixels are blanked if the integrated intensity is less than 5 K km s⁻¹ ($\sim 5\sigma$) for each integrated velocity range. The lowest contour levels and the contour intervals are 5.0 K km s⁻¹. The integrated intensities (contours) of the three components are superposed on the Herschel 160 μm continuum image (Molinari et al. 2016) for the (d) 22 km s⁻¹, (e) 27 km s⁻¹, and (f) 33 km s⁻¹ clouds. The lowest contour levels and the contour intervals are 8.0 K km s⁻¹ and 15.0 K km s⁻¹ for (d), 13.0 K km s⁻¹ and 15.0 K km s⁻¹ for (e), 10.0 K km s⁻¹ and 15.0 K km s⁻¹ for (f). The crosses and dotted circles are the same as in Figure 1(b)

4.5 Physical parameters of the molecular gas

Table 4. Excitation temperature, optical depth, and column density of molecular clouds in Vul OB1.

Name	T_{ex} [K]	τ_{13}	τ_{18}	$N_{\text{X}}^{12} \text{ max}$ [cm ⁻²]	$N_{\text{X}}^{12} \text{ mean}$ [cm ⁻²]	$N_{\text{LTE}}^{13} \text{ max}$ [cm ⁻²]	$N_{\text{LTE}}^{13} \text{ mean}$ [cm ⁻²]	$N_{\text{LTE}}^{18} \text{ max}$ [cm ⁻²]	$N_{\text{LTE}}^{18} \text{ mean}$ [cm ⁻²]
(1)	(2)	(3)	(4)	(5)	(6)	(7)	(8)	(9)	(10)
Sh2-86	10	0.38	0.13	4.4×10^{22}	8.0×10^{21}	1.1×10^{23}	1.1×10^{22}	7.4×10^{22}	1.6×10^{22}
22 km s ⁻¹ cloud	10	0.38	0.13	2.9×10^{22}	5.3×10^{21}	1.0×10^{23}	1.1×10^{22}	7.4×10^{22}	1.7×10^{22}
27 km s ⁻¹ cloud	10	0.38	0.1	2.2×10^{22}	4.6×10^{21}	7.0×10^{22}	7.7×10^{21}	5.3×10^{22}	1.6×10^{22}
32 km s ⁻¹ cloud	8.8	0.41	0.19	1.2×10^{22}	2.8×10^{21}	1.8×10^{22}	2.4×10^{21}	1.7×10^{22}	1.0×10^{22}
Sh2-87	18	0.27	0.04	6.0×10^{22}	1.6×10^{22}	2.0×10^{23}	3.7×10^{22}	8.0×10^{22}	3.4×10^{22}
Sh2-88	13	0.39	0.09	6.4×10^{22}	1.2×10^{22}	2.7×10^{23}	2.7×10^{22}	1.5×10^{23}	2.6×10^{22}

Note: The mean values were adopted within the cloud surface area (S). Columns: (1) Name. (2) The mean excitation temperature obtained from the ¹²CO peak intensity. (3) The mean optical depth obtained from ¹³CO. (4) The same as (3), but for C¹⁸O. (5) The peak H₂ column density derived from ¹²CO assuming the X-factor. (6) The mean H₂ column density calculated from ¹²CO assuming the X-factor. (7) The same as (6), but for ¹³CO assuming LTE. (8) The same as (6), but for ¹³CO, assuming LTE. (9) The same as (7), but for C¹⁸O. (10) The same as (8), but for C¹⁸O.

Table 5. Size and molecular mass in Vul OB1.

Name	D_{12} [pc]	M_{X}^{12} [M_{\odot}]	D_{13} [pc]	M_{LTE}^{13} [M_{\odot}]	D_{18} [pc]	M_{LTE}^{18} [M_{\odot}]
(1)	(2)	(3)	(4)	(5)	(6)	(7)
Sh2-86	43	8.0×10^4	15	4.3×10^4	3.5	3.4×10^3
22 km s ⁻¹ component	31	2.9×10^4	10	1.7×10^4	3	1.8×10^3
27 km s ⁻¹ component	34	4.5×10^4	13	2.3×10^4	2	1.3×10^3
32 km s ⁻¹ component	22	1.4×10^4	10	4.1×10^3	0.7	78
Sh2-87	7.4	6.5×10^3	3.6	8.4×10^3	1.1	7.8×10^2
Sh2-88	15	1.1×10^4	4.9	1.1×10^4	1.6	1.2×10^3

Note: The physical parameters were calculated using the data points above 5σ (~ 3.5 K for ¹²CO and 0.90 K for ¹³CO and C¹⁸O $J=1-0$). Columns: (1) Name. (2) The ¹²CO cloud diameter within 10% of the peak integrated intensity. (3) The total molecular mass estimated from ¹²CO. (4) The same as (2), but for ¹³CO. (5) The same as (3), but for ¹³CO. (6) The same as (2), but for C¹⁸O. (7) The same as (3), but for C¹⁸O.

We derived the physical parameters of the molecular clouds in Vul OB1 following a procedure that uses the X-factor and assumes local thermal equilibrium (LTE), which is described by Pineda et al. (2008); Wilson et al. (2013), and Sofue & Kohno (2020).

The brightness temperature $T_{\text{B}}(v)$ can be expressed in terms of the excitation temperature T_{ex} and the optical depth $\tau(v)$, and it is given by

$$T_{\text{B}}(v) = T_0 \left(\frac{1}{\exp(T_0/T_{\text{ex}}) - 1} - \frac{1}{\exp(T_0/T_{\text{bg}}) - 1} \right) (1 - \exp(-\tau(v))), \quad (3)$$

where T_0 is the Planck temperature defined as $T_0 = \frac{h\nu}{k}$, with k and h being the Boltzmann and Planck constants, respectively, and T_{bg} is the black-body temperature of the cosmic microwave background: $T_{\text{bg}} = 2.725$ K.

If we assume that the ¹²CO $J=1-0$ line is optically thick ($\tau \rightarrow \infty$), the excitation temperature is given by

$$T_{\text{ex}} = 5.53 / \ln \left(1 + \frac{5.53}{T_{\text{B}}(^{12}\text{CO})_{\text{max}}/\text{K} + 0.836} \right) [\text{K}], \quad (4)$$

where $T_{\text{B}}(^{12}\text{CO})_{\text{max}}$ is the peak brightness temperature. This yields mean values $T_{\text{ex}} \sim 10 - 18$ K in Vul OB1 and in each H II region.

The ¹³CO and C¹⁸O optical depths can be derived from the brightness temperatures and the excitation temperature, and they are given by

$$\tau_0^{13} = -\ln \left[1 - \frac{T_{\text{B}}(^{13}\text{CO})_{\text{max}}}{5.29 \text{ K}} \left\{ \frac{1}{\exp(\frac{5.29 \text{ K}}{T_{\text{ex}}}) - 1} - 0.168 \right\}^{-1} \right] \text{ and} \quad (5)$$

$$\tau_0^{18} = -\ln \left[1 - \frac{T_B(\text{C}^{18}\text{O})_{\max}}{5.27 \text{ K}} \left\{ \frac{1}{\exp(\frac{5.27 \text{ K}}{T_{\text{ex}}}) - 1} - 0.169 \right\}^{-1} \right], \text{ respectively.} \quad (6)$$

The values τ_0^{13} and τ_0^{18} at the peak intensity were thus found to be ~ 0.3 - 0.4 and ~ 0.04 - 0.19 , respectively, for each H II region. In terms of the brightness temperature and the velocity width (dv), the ^{13}CO and C^{18}O column densities are given by

$$\begin{aligned} N(^{13}\text{CO}) &= 2.42 \times 10^{14} \frac{T_{\text{ex}}/\text{K}}{1 - \exp(-\frac{5.29 \text{ K}}{T_{\text{ex}}})} \int \tau^{13}(v) dv \\ &\sim 2.42 \times 10^{14} \frac{\tau_0^{13}}{1 - \exp(-\tau_0^{13})} \frac{1}{1 - \exp(-\frac{5.29 \text{ K}}{T_{\text{ex}}})} \int T_B(^{13}\text{CO})(v) dv [\text{cm}^{-2}], \end{aligned} \quad (7)$$

$$\begin{aligned} N(\text{C}^{18}\text{O}) &= 2.52 \times 10^{14} \frac{T_{\text{ex}}/\text{K}}{1 - \exp(-\frac{5.27 \text{ K}}{T_{\text{ex}}})} \int \tau^{18}(v) dv \\ &\sim 2.52 \times 10^{14} \frac{\tau_0^{18}}{1 - \exp(-\tau_0^{18})} \frac{1}{1 - \exp(-\frac{5.27 \text{ K}}{T_{\text{ex}}})} \int T_B(\text{C}^{18}\text{O})(v) dv [\text{cm}^{-2}], \end{aligned} \quad (8)$$

where we use the relationship $T_{\text{ex}} \int \tau(v) dv \sim \frac{\tau_0}{1 - \exp(-\tau_0)} \int T_B(v) dv$ and assumes the optically thin case quoted from Wilson et al. (2013).

The H_2 column density is derived from the ^{12}CO integrated intensity using the X-factor ($X(^{12}\text{CO})$). The ^{13}CO , and C^{18}O column densities are calculated from the isotopic abundance ratios using the following formulas:

$$N_X^{12}(\text{H}_2) = X(^{12}\text{CO}) \int T_B(^{12}\text{CO}) dv, \quad (9)$$

$$N_{\text{LTE}}^{13}(\text{H}_2) = Y[^{13}\text{CO}] \times N(^{13}\text{CO}), \quad (10)$$

$$N_{\text{LTE}}^{18}(\text{H}_2) = Y[\text{C}^{18}\text{O}] \times N(\text{C}^{18}\text{O}). \quad (11)$$

We used $2.0 \times 10^{20} [(\text{K kms}^{-1})^{-1} \text{ cm}^{-2}]$ as the X-factor whose uncertainty is 30%. (Bolatto et al. 2013). The adopted CO conversion factors for $Y[^{13}\text{CO}]$ and $Y[\text{C}^{18}\text{O}]$ are 7.7×10^5 and 5.6×10^6 , respectively. These values are calculated from the isotopic abundance ratios $[^{12}\text{C}]/[^{13}\text{C}] = 77$, and $[^{16}\text{O}]/[^{18}\text{O}] = 560$ (Wilson, & Rood 1994), and H_2 abundance ratio $[^{12}\text{CO}]/[\text{H}_2] = 10^{-4}$ (e.g., Frerking et al. 1982; Pineda et al. 2010). The peak column densities obtained from ^{13}CO are $> 10^{23} \text{ cm}^{-2}$, which is larger than that estimated from ^{12}CO . This tendency is consistent with the other GMCs in the Milky Way (e.g., Sofue & Kohno 2020).

We estimated the diameter D of each molecular cloud using the equation

$$D = 2\sqrt{\frac{S}{\pi}}, \quad (12)$$

where S is the cloud area within 10% of the peak integrated intensity. The resulting diameters of the clouds in Sh 2-86, Sh 2-87, and Sh 2-88 obtained by ^{12}CO are ~ 40 pc, ~ 7 pc, and ~ 15 pc, respectively.

The total molecular mass is given by

$$M = \mu_{\text{H}_2} m_{\text{H}} d^2 \sum_i \Omega N_i(\text{H}_2), \quad (13)$$

where $\mu_{\text{H}_2} \sim 2.8$ is the mean molecular weight of a hydrogen molecule including contribution of helium (e.g., Appendix A.1. of Kauffmann et al. 2008), $m_{\text{H}} = 1.67 \times 10^{-24} \text{ g}$ is the proton mass, d is the distance to the Vul OB1 GMC, Ω is the solid angle of the map pixel, and $N_i(\text{H}_2)$ is the molecular column density of the i -th pixel. The total mass of Sh 2-86, Sh 2-87, and Sh 2-88 are 8.0×10^4 , 6.5×10^3 , and $1.1 \times 10^4 M_{\odot}$ derived by ^{12}CO . The mass derived from ^{12}CO and ^{13}CO is consistent with this within a factor of 2-3. On the other hand, the mass derived from C^{18}O is about smaller than one order of magnitude. This difference causes the C^{18}O line to be optically thin and trace the dense region in the Vul OB1 GMC. These results are consistent with molecular clouds in the Galactic Plane revealed by the FUGIN CO survey (see Figure 13 of Torii et al. 2019). We summarize the physical parameters of molecular clouds in Vul OB1 in Table 4 and 5.

5 Discussion

5.1 Comparison of the H₂ column density with YSO distributions

Figure 8(a) shows the spatial distribution of the YSOs cataloged by Billot et al. (2010) superposed on the H₂ column density map derived from the ¹²CO $J = 1-0$ integrated intensity using the X-factor $X(\text{CO}) = 2.0 \times 10^{20} [(\text{K km s}^{-1})^{-1} \text{ cm}^{-2}]$ (Bolatto et al. 2013). The column density is high ($> 1.0 \times 10^{22} \text{ cm}^{-2}$) near IRAS 19410+2336 and NGC 6823. Figure 8(b) presents the surface density of YSOs and OB-type stars (red contours) superposed on the H₂ column density map. We calculated the surface density of stars at each point of a $10''$ grid using the nearest neighbor method (Chavarría et al. 2008; Billot et al. 2010). The equation of the surface density (σ_{star}) is given by

$$\sigma_{\text{star}} = \frac{N}{\pi r_N^2} [\text{stars pc}^{-2}], \quad (14)$$

where r_N is the distance to the nearest neighbor. In this paper, we adopted $N = 5$, the same as Billot et al. (2010). The surface density map was convolved to $1'$ with a Gaussian kernel function. We point out that the YSOs and OB-type stars are concentrated around the NGC 6823 cluster. Billot et al. (2010) argue that each YSO-population class is homogenously distributed in Vul OB1, and they were unable to determine the age sequence. Hence, they excluded the propagating star formation scenario proposed by Ehlerová et al. (2001). However, we note that the YSOs around SNR G59.5+0.1 may have been induced by the stellar wind from the G59.5+0.1 progenitor, as suggested by Xue, & Wu (2008). Based on our observational results and previous studies, we discuss the cluster formation scenario in NGC 6823 in the following subsection.

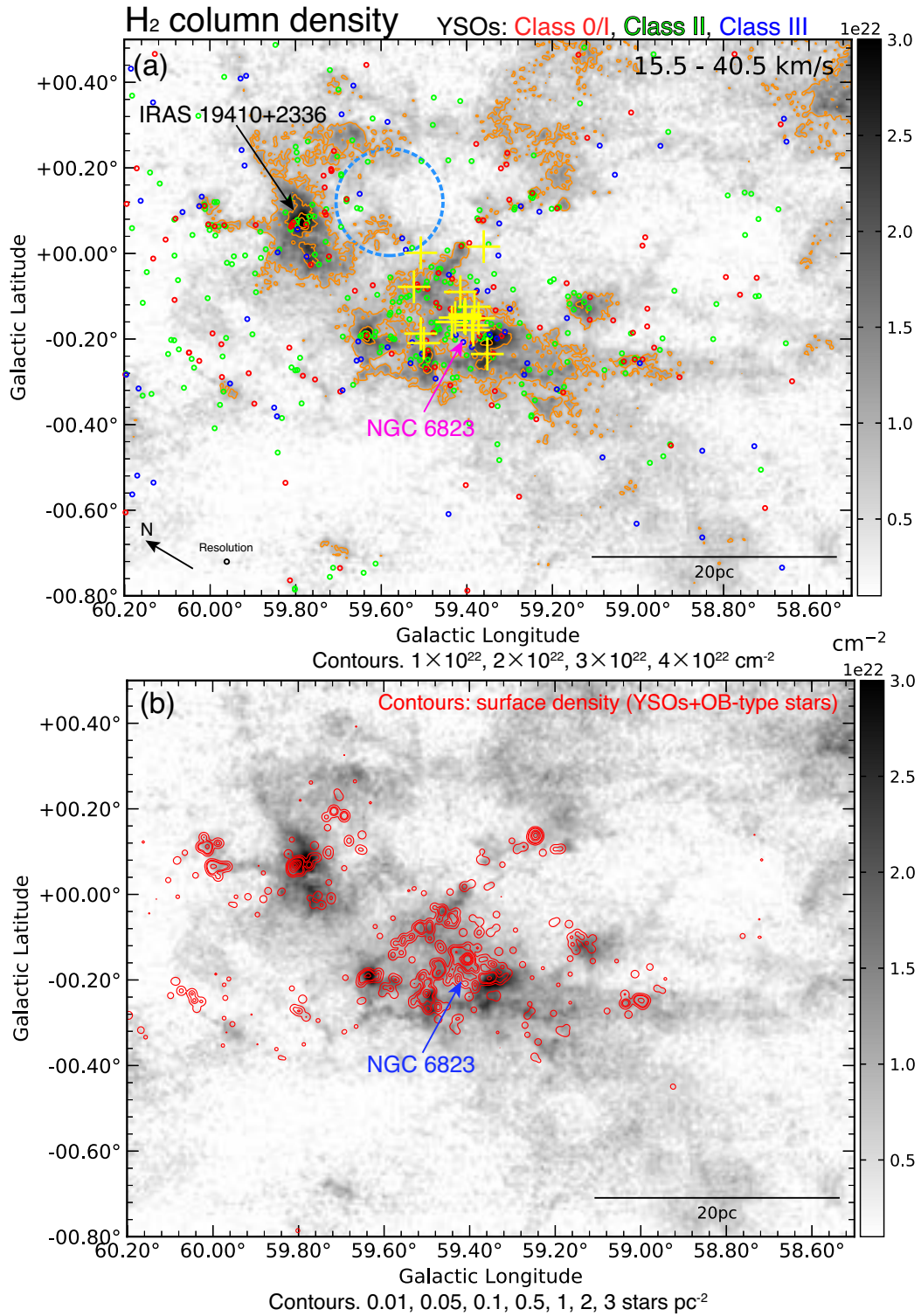


Fig. 8. (a) The YSO distributions superposed on the H_2 column density maps derived from the $^{12}\text{CO } J=1-0$ data. The contour levels for the column density are 1×10^{22} , 2×10^{22} , 3×10^{22} , and $4 \times 10^{22} \text{ cm}^{-2}$. Red, green, and blue circles indicate the class 0/I, class II, and class III objects, respectively, as identified by Billot et al. (2010). The yellow crosses indicate the OB-type stars in NGC 6823 identified by Massey et al. (1995). The blue dotted circle shows the position of SNR G59.5+0.1 (Green 2019). (b) The surface density of YSOs and OB-type stars (red contours) superposed on the H_2 column density map. The red contours were convolved to $1'$ with a Gaussian kernel function. The contour levels for the surface density are 0.01, 0.05, 0.1, 0.5, 1, 2, and 3 stars pc^{-2} . The column density map resolution after convolution is $40''$.

5.2 The interpretations of the three velocity components associated with Sh 2-86

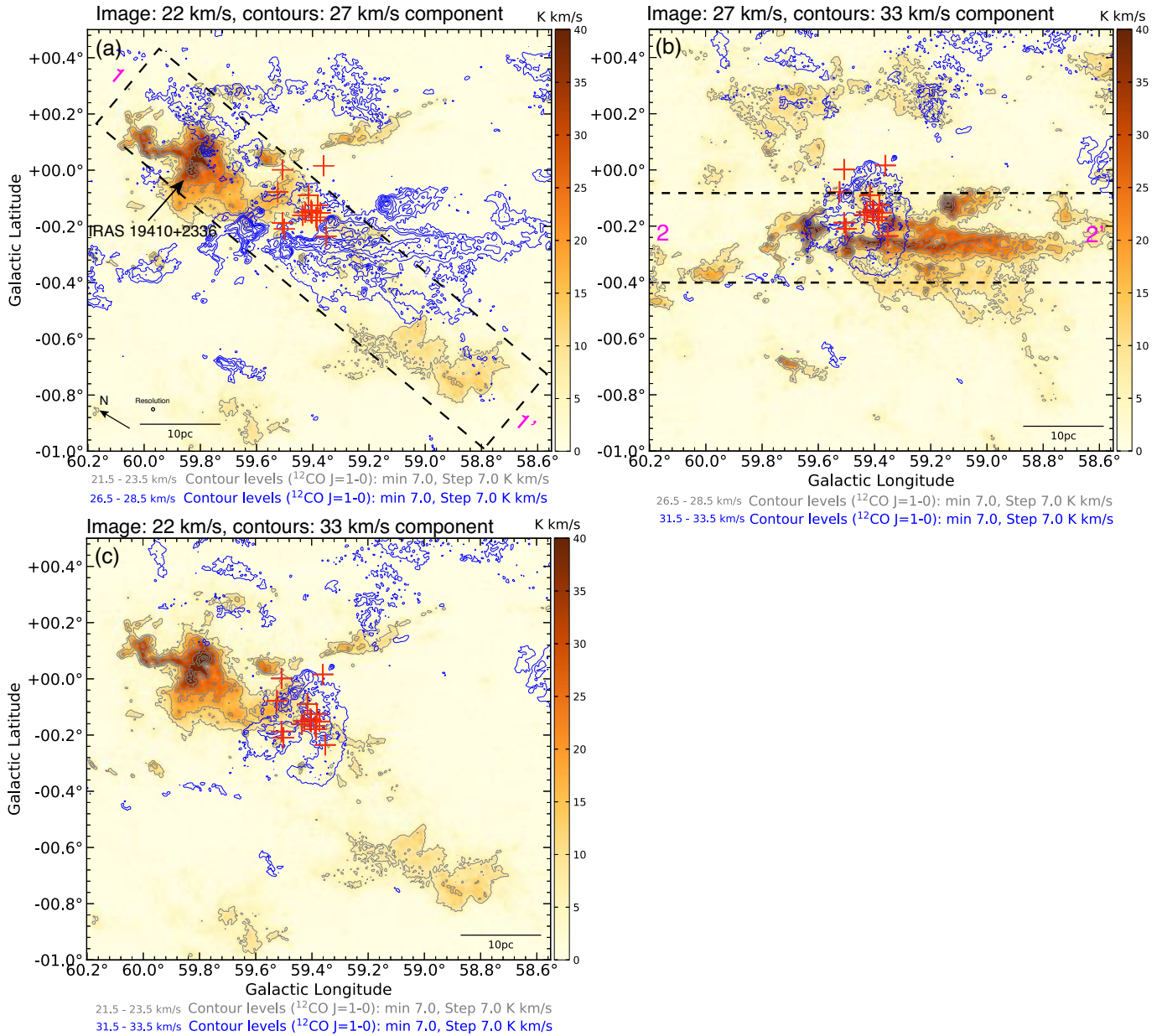


Fig. 9. Spatial distributions of the $^{12}\text{CO } J=1-0$ emission integrated over two different velocity ranges. (a) The 22 km s⁻¹ (image) and 27 km s⁻¹ (blue contours) components. (b) The 27 km s⁻¹ (image) and 33 km s⁻¹ (blue contours) components. Black dotted boxes shows the making ranges of the position-velocity diagram along the filaments in Figure 10(a) and (b). (c) The 22 km s⁻¹ (image) and 33 km s⁻¹ (blue contours) components. The lowest contour levels and the contour intervals are 7.0 K km s⁻¹. The crosses are the same as in Figure 8. The map resolution after convolution is 40''.

Figure 9 presents the $^{12}\text{CO } J=1-0$ integrated intensity maps for the two overlapping clouds associated with Sh 2-86. The 27 km s⁻¹ cloud has peaks at the southern side of the cluster, corresponding to the intensity depression of the 22 km s⁻¹ cloud (Figure 9a). That shows anti-correlated spatial distributions. The NGC 6823 cluster members are found to be the overlap region between the 33 km s⁻¹ cloud and 22, 27 km s⁻¹ components (Figure 9b, c). These components are also connected in the position-velocity diagram (see Figure 10).

Molecular clouds associated with massive star-forming regions often compose of multiple velocity components. They are interpreted as the expansion by stellar wind (e.g., Deharveng et al. 2010), oscillation of a single cloud (e.g., Lada et al. 2003), infall motion of a massive cloud (e.g., Shimoikura et al. 2016; Shimoikura et al. 2018), and a cloud-cloud collision (e.g., Kohno et al. 2021a, 2021b). To investigate the origin of three velocity components in detail, we made the position-velocity diagram along with

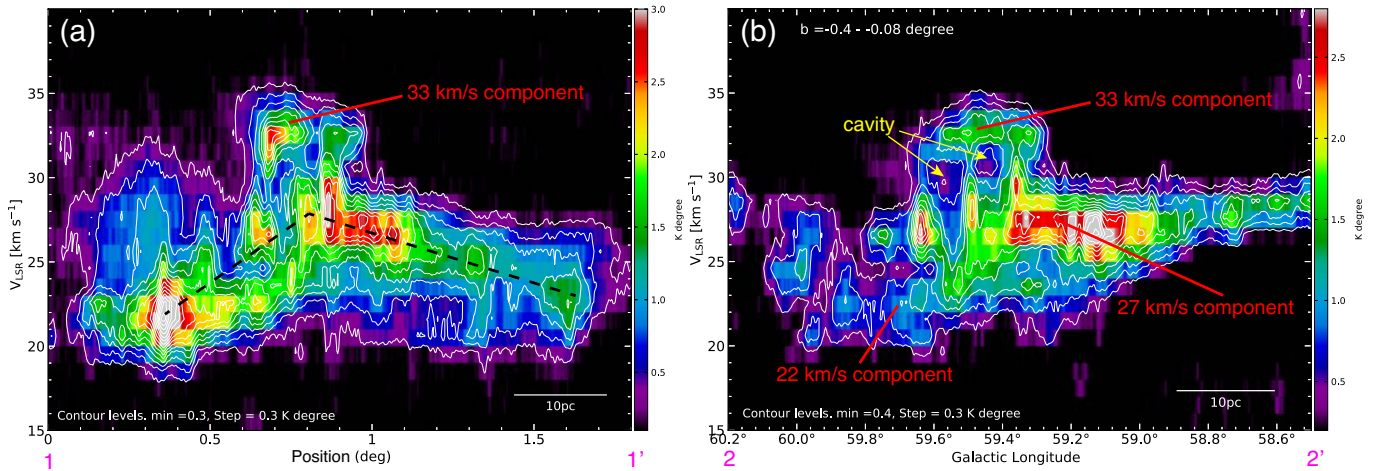


Fig. 10. (a) Position-velocity diagram for ^{12}CO integrated along the Filament B (cut 1-1' in Figure 9a). The lowest contours and intervals are 0.3 K degree and 0.3 K degree, respectively. (b) The same as (a), but along the Filament C (cut 2-2' in Figure 9b). The lowest contours and intervals are 0.4 K degree and 0.3 K degree, respectively.

the elongation of Filament B and C as shown in Figure 10(a) and (b), respectively. Billot et al. (2010) and Chapin et al. (2008) pointed out that the ionization feedback by the stellar wind from the OB-type stars in the NGC 6823 cluster affects the parent molecular cloud of Sh 2-86. The two cavity structures having <5 pc exist at $\sim 31 \text{ km s}^{-1}$ presented in Figure 10(b). We suggest that they were formed by the ionization effect of the NGC 6823 cluster. On the other hand, the 22 km s^{-1} component exists 5 km s^{-1} apart from the cavity velocity and distributes at the blue-shifted side of the 27 km s^{-1} component. The 22 km s^{-1} component also has an intensity peak at IRAS 19410+2336, which is located ~ 15 pc away from the NGC 6823 cluster (Figure 9a). Therefore, we suggest that the effect of stellar feedback by the NGC 6823 cluster toward the 22 km s^{-1} component is limited.

Shimoikura et al. (2016) reported the two velocity components having the velocity separation of $\sim 1 \text{ km s}^{-1}$ associated with the massive clump of S235 AB. They showed symmetrical two peaks with the clump center at the position-velocity diagram taken along its major axis (see Figure 3b in Shimoikura et al. 2016). The authors argued that their velocity distribution is interpreted as the infall motion of a single massive cloud with rotation based on the model of single protostars presented by Ohashi et al. (1997) (see also Type 2 massive clumps presented by Shimoikura et al. 2018). In the case of Sh 2-86, we find the inverted V-shaped structure (Figure 10a) and three intensity peaks (Figure 10b) on the position-velocity diagrams along with Filament B and Filament C, respectively. These features are different from the velocity gradients reported by Shimoikura et al. (2016). Hence, we suggest that the infall motion with rotation of the GMC scale is unlikely to explain our observational results.

Lada et al. (2003) proposed that the oscillation of a single cloud can explain the origin of the velocity gradient in the molecular cloud associated with the starless core Barnard 68. If the cloud has oscillation, we are likely to find the velocity pattern like the sine wave on the position-velocity diagram along the filament (e.g., Figure 6 in Liu et al. 2019). However, we cannot find them on the position-velocity diagram in Sh 2-86. Thus, we suggest that it is difficult for the cloud oscillation (pulsation) to explain the origin of the three independent velocity components associated with Sh 2-86.

Based on our CO data, we show the connecting the three velocity components in the position-velocity diagram, V-shape structure, complementary spatial distributions, and high-intensity ratio around the NGC 6823 cluster. We propose that these observational signatures show the evidences of cloud-cloud collisions (see also the review paper by Fukui et al. 2021). Numerical simulations of cloud-cloud collisions reproduced the (inverted) V-shaped structures (see Figure 5 middle panel in Haworth et al. 2015), and anti-correlated spatial distributions of different velocity channels (Matsumoto et al. 2015). Arzoumanian et al. (2018) also argue that V-shaped structure shows the shock compression for the filament formation by colliding flows. Theoretical studies have also demonstrated that cloud-cloud collisions can set up the initial conditions for massive cluster star formation (e.g., Habe & Ohta 1992; Inoue & Fukui 2013; Inoue et al. 2018; Takahira et al. 2014; Wu et al. 2015). The radio observations were also suggested that cloud-cloud collisions (e.g., Sagittarius B2: Hasegawa et al. 1994, M20: Torii et al. 2011, RCW 38: Fukui et al. 2016, IRAS 05358+3543: Yamada et al. 2021) and filament-filament collisions (e.g., Serpens South: Nakamura et al. 2014, Cygnus OB 7: Dobashi et al. 2014) as a trigger of massive stars and cluster formation in the Milky Way. These results were also supported by the recent observational studies of Large Magellanic Cloud (e.g., Fukui et al. 2015; Saigo et al. 2017; Fukui et al. 2019; Tokuda et al. 2019), M33 (e.g., Sano et al. 2021) and Antennae Galaxies (e.g., Tsuge et al. 2021; Tsuge et al. 2021).

Xue, & Wu (2008) and Higuchi et al. (2010) argue that the clump-clump collision triggered the cluster formation of Sh 2-87 and Sh 2-88 in Vul OB1. In the case of Sh 2-86, it is excited by the 17 OB-type stars in the NGC 6823 cluster (see Table 2). This H II region is also the most active star-forming site in Vul OB1 (Billot et al. 2010). We suggest that multiple collisions between molecular cloud and GMFs having high peak column density $\sim 1 \times 10^{23} \text{ cm}^{-2}$ obtained by ^{13}CO are likely to explain the origin of the multiple OB-type star formation in Vul OB1. The dynamical collision timescale is estimated to be 20-30 pc/ ($5 \text{ km s}^{-1} \times \sqrt{2}$) ~ 3 -4 Myr, assuming a viewing angle of 45° . This value is roughly consistent with the cluster age of NGC 6823 (3 ± 1 Myr: Pigulski et al. 2000). Therefore, we propose multiple cloud collisions are the most plausible hypothesis to explain the origin of the three velocity components and OB-type stars in Sh 2-86. To advance our current understanding in Vul OB 1, additional molecular line observations using shock tracers, such as SiO (Fujita et al. 2021b; Cosentino et al. 2020) and dense gas tracers (Priestley & Whitworth 2021), are helpful, leading the dynamical state as a consequence of the molecular cloud collisions.

5.3 The origin of the filamentary clouds in the Local Spur of the Milky Way

Table 6. Comparison with physical parameters of GMFs as sites of a cloud-cloud collision

Name	Length [pc]	Width [pc]	v_{FWHM} [km s^{-1}]	$N(\text{H}_2)_{\text{peak}}$ [cm^{-2}]	Total mass [M_\odot]	M_{line} [M_\odot/pc]	Reference
(1)	(2)	(3)	(4)	(5)	(6)	(7)	(8)
Filament C in Sh 2-86	~ 30	~ 5	~ 3	1×10^{22}	$\sim 4 \times 10^4$	$\sim 1 \times 10^3$	This work
HVS in W51*	~ 90	~ 10	~ 5	2×10^{22}	$\sim 3 \times 10^5$	$\sim 3 \times 10^3$	Fujita et al. (2021a)
Filament B in GMC-16 †	~ 70	~ 5 -6	~ 4	5×10^{22}	$\sim 4 \times 10^5$	$\sim 6 \times 10^3$	Tokuda et al. (2020)

* The parameters of the W51 GMC was taken from the FUGIN CO survey data (Umemoto et al. 2017; Fujita et al. 2021a; URL: <https://nro-fugin.github.io>).

† The parameters of Filament B in GMC-16 of M33 were obtained by the $^{12}\text{CO } J=2-1$ data. We applied the X(CO) factor of $4 \times 10^{20} \text{ [K km s}^{-1}\text{]}^{-1} \text{ cm}^{-2}$ and the $^{12}\text{CO } J=2-1/1-0$ intensity ratio of 0.7 (Gratier et al. 2010; Druard et al. 2014). More detailed information is described in Tokuda et al. (2020) and Kondo et al. (2021).

Columns: (1) Name. (2) The GMF length. (3) The GMF width. (4) The FWHM ($2\sigma\sqrt{2\ln 2}$) of peak spectra by a single Gaussian fitting, where σ is the standard deviation of the line profile. (5) The H_2 peak column density assuming the X-factor. (6) The total molecular mass derived by ^{12}CO . (7) Line mass obtained by the total mass divided GMF length. (8) Reference.

In particular, Filament C in the 27 km s^{-1} cloud is distributed along the Galactic plane. This feature is common to the high-velocity stream (HVS) in the W51 GMC (Fujita et al. 2021a). A galactic spiral density wave has been suggested as the origin of the HVS (e.g. Burton 1970; Carpenter & Sanders 1998; Koo 1999; Kumar et al. 2004). Recently, Tokuda et al. (2020) discovered the GMFs associated with the high-mass star-forming region in the external spiral galaxy M33. The authors suggested that a Galactic spiral shock had formed these GMFs. Table 6 shows the comparison of Filament C with the physical parameters of GMFs as sites of a cloud-cloud collision. Filament C has $\sim 1/2$ - $1/3$ length comparing with HVS and GMC-16. This value is also smaller than other GMFs identified by previous studies with ~ 100 pc in the Galactic plane (e.g., Jackson et al. 2010; Ragan et al. 2014). The total mass is $\sim 1/10$ of HVS and GMC-16. Therefore, we suggest that Filament C at the Local spur of the Milky Way is the smaller scale GMF than reported by previous studies.

On the other hand, based on the observations of the external spiral galaxy M51 (e.g., Koda et al. 2009; Miyamoto et al. 2014), it has been suggested that filamentary clouds in inter-arm regions can be produced by galactic shear motions. Numerical simulations by Wada & Koda (2004) and Dobbs & Bonnell (2006) have reproduced such filamentary structures in inter-arm regions. Hence, we suggest that they are formed by galactic-scale dynamics like spiral shocks or shear motions. More detailed analyses are necessary to confirm the origins of the GMFs in Sh 2-86. With such detailed considerations, we will argue the separated paper.

6 Summary

The conclusions of this paper are as follows:

1. We have performed large-scale ^{12}CO , ^{13}CO , and $\text{C}^{18}\text{O } J=1-0$ observations toward the Vulpecula OB association ($l \sim 60^\circ$) as a part of the Nobeyama 45 m Local Spur CO survey project, with the goal of determining the cause of cluster formation in an inter-arm region of the Milky Way.
2. The molecular clouds are distributed over ~ 100 pc, and they have peaks at the HII regions Sh 2-86, Sh 2-87, and Sh 2-88 in Vul OB1. The whole of Vul OB1 is located in the Local Spur between the Local Arm and the Sagittarius Arm of the Milky Way.
3. We discovered new GMFs in Sh 2-86, which have a length of ~ 30 pc, width of ~ 5 pc, and mass of $\sim 4 \times 10^4 M_\odot$ obtained by

^{12}CO .

4. Sh 2-86 contains three velocity components at 22, 27, and 33 km s⁻¹. These clouds have high intensity-ratios around high-mass stars, and they coincide with to the infrared dust emission. Therefore, we conclude that the multiple velocity components are likely to be physically associated with Sh 2-86.
5. The OB-type stars in the open cluster NGC 6823 are located at the intersection of three clouds. From these observational results, we suggest that the cloud-cloud collision scenario can explain the origin of cluster formation in the Vul OB1 GMC.
6. We propose that the GMFs in Vul OB1 were produced by galactic-scale dynamics like spiral shocks or shear motions.

Acknowledgements

The authors are grateful to the referee for thoughtful comments on the paper. We are grateful to Mr. Rin Yamada of Nagoya University for a useful discussion.

The Nobeyama 45-m radio telescope is operated by Nobeyama Radio Observatory, a branch of the National Astronomical Observatory of Japan. Herschel is an ESA space observatory with science instruments provided by European-led Principal Investigator consortia and with important participation from NASA. PACS has been developed by a consortium of institutes led by MPE (Germany) and including UVIE (Austria); KU Leuven, CSL, IMEC (Belgium); CEA, LAM (France); MPIA (Germany); INAF-IFSI/OAA/OAP/OAT, LENS, SISSA (Italy); IAC (Spain). This development has been supported by the funding agencies BMVIT (Austria), ESA-PRODEX (Belgium), CEA/CNES (France), DLR (Germany), ASI/INAF (Italy), and CICYT/MCYT (Spain). SPIRE has been developed by a consortium of institutes led by Cardiff University (UK) and including Univ. Lethbridge (Canada); NAOC (China); CEA, LAM (France); IFSI, Univ. Padua (Italy); IAC (Spain); Stockholm Observatory (Sweden); Imperial College London, RAL, UCL-MSSL, UKATC, Univ. Sussex (UK); and Caltech, JPL, NHSC, Univ. Colorado (USA). This development has been supported by national funding agencies: CSA (Canada); NAOC (China); CEA, CNES, CNRS (France); ASI (Italy); MCINN (Spain); SNSB (Sweden); STFC, UKSA (UK); and NASA (USA)."

The work is financially supported by a Grant-in-Aid for Scientific Research (KAKENHI, No. 18K13580,) from MEXT (the Ministry of Education, Culture, Sports, Science and Technology of Japan) and JSPS (Japan Society for the Promotion of Science).

The authors would like to thank Enago (www.enago.jp) for the English language review.

Software: We utilized Astropy, a community-developed core Python package for astronomy (Astropy Collaboration et al. 2013; Astropy Collaboration et al. 2018), NumPy (van der Walt et al. 2011), Matplotlib (Hunter 2007), IPython (Perez, & Granger 2007), APLpy (Robitaille & Bressert 2012), Miriad (Sault et al. 1995), and Montage⁴ software (Berriman & Good 2017).

This research made use of Montage. It is funded by the National Science Foundation under Grant Number ACI-1440620, and was previously funded by the National Aeronautics and Space Administration's Earth Science Technology Office, Computation Technologies Project, under Cooperative Agreement Number NCC5-626 between NASA and the California Institute of Technology.

Appendix 1 ^{13}CO and C^{18}O velocity channel maps of Sh 2-86

We present the velocity channel maps of the ^{13}CO and C^{18}O $J = 1-0$ emissions toward Sh 2-86 in the Appendix 1 (see Figures 11 and 12)

References

- | | |
|--|---|
| <p>Abreu-Vicente, J., Ragan, S., Kainulainen, J., et al. 2016, <i>A&A</i>, 590, A131. doi:10.1051/0004-6361/201527674</p> <p>Astropy Collaboration, Robitaille, T. P., Tollerud, E. J., et al. 2013, <i>A&A</i>, 558, A33</p> <p>Astropy Collaboration, Price-Whelan, A. M., Sipőcz, B. M., et al. 2018, <i>AJ</i>, 156, 123</p> <p>Arzoumanian, D., Shimajiri, Y., Inutsuka, S.-. ichiro ., et al. 2018, <i>PASJ</i>, 70, 96. doi:10.1093/pasj/psy095</p> <p>Barkhatova, K. A. 1957, <i>Soviet Ast.</i>, 1, 822</p> <p>Barsony, M. 1989, <i>ApJ</i>, 345, 268</p> <p>Berriman, G. B. & Good, J. C. 2017, <i>PASP</i>, 129, 058006. doi:10.1088/1538-3873/aa5456</p> | <p>Beuther, H., Schilke, P., & Wyrowski, F. 2004, <i>ApJ</i>, 615, 832</p> <p>Bica, E., Bonatto, C., & Dutra, C. M. 2008, <i>A&A</i>, 489, 1129</p> <p>Billot, N., Noriega-Crespo, A., Carey, S., et al. 2010, <i>ApJ</i>, 712, 797</p> <p>Blitz, L., Fukui, Y., Kawamura, A., et al. 2007, <i>Protostars and Planets V</i>, 81</p> <p>Bolatto, A. D., Wolfire, M., & Leroy, A. K. 2013, <i>ARA&A</i>, 51, 20</p> <p>Burton, W. B. 1970, <i>A&AS</i>, 2, 291</p> <p>Burton, W. B. & Gordon, M. A. 1978, <i>A&A</i>, 63, 7</p> <p>Cappa, C., Pineault, S., Arnal, E. M., et al. 2002, <i>A&A</i>, 395, 955</p> <p>Carpenter, J. M. & Sanders, D. B. 1998, <i>AJ</i>, 116, 1856</p> <p>Chapin, E. L., Ade, P. A. R., Bock, J. J., et al. 2008, <i>ApJ</i>, 681, 428</p> <p>Chavarría, L. A., Allen, L. E., Hora, J. L., et al. 2008, <i>ApJ</i>, 682, 445. doi:10.1086/588810</p> |
|--|---|

⁴ <http://montage.ipac.caltech.edu>

- Chen, Y., Zheng, X.-W., Yao, Y., et al. 2003, *A&A*, 401, 185
- Cohen, R. S., Cong, H., Dame, T. M., et al. 1980, *ApJL*, 239, L53
- Collinder, P. 1931, *Annals of the Observatory of Lund*, 2, B1
- Combes, F. 1991, *ARA&A*, 29, 195
- Cosentino, G., Jiménez-Serra, I., Henshaw, J. D., et al. 2020, *MNRAS*, 499, 1666. doi:10.1093/mnras/staa2942
- Dame, T. M., & Thaddeus, P. 1985, *ApJ*, 297, 751
- Dame, T. M., Elmegreen, B. G., Cohen, R. S., et al. 1986, *ApJ*, 305, 892
- Dame, T. M., Ungerechts, H., Cohen, R. S., et al. 1987, *ApJ*, 322, 706
- Deharveng, L., & Maucherat, M. 1978, *A&A*, 70, 19
- Deharveng, L., Nadeau, D., Zavagno, A., et al. 2000, *A&A*, 360, 1107
- Deharveng, L., Schuller, F., Anderson, L. D., et al. 2010, *A&A*, 523, A6. doi:10.1051/0004-6361/201014422
- Dobashi, K., Matsumoto, T., Shimoikura, T., et al. 2014, *ApJ*, 797, 58. doi:10.1088/0004-637X/797/1/58
- Dobbs, C. L. & Bonnell, I. A. 2006, *MNRAS*, 367, 873
- Dobbs, C. L., Krumholz, M. R., Ballesteros-Paredes, J., et al. 2014, *Protostars and Planets VI*, 3
- Druard, C., Braine, J., Schuster, K. F., et al. 2014, *A&A*, 567, A118. doi:10.1051/0004-6361/201423682
- Duarte-Cabral, A. & Dobbs, C. L. 2017, *MNRAS*, 470, 4261. doi:10.1093/mnras/stx1524
- Evans, N. J., Blair, G. N., Harvey, P., et al. 1981, *ApJ*, 250, 200
- Ehlerová, S., Palouš, J., & Huchtmeier, W. K. 2001, *A&A*, 374, 682
- Elmegreen, B. G., & Lada, C. J. 1977, *ApJ*, 214, 725
- Erickson, R. R. 1971, *A&A*, 10, 270
- Frerking, M. A., Langer, W. D., & Wilson, R. W. 1982, *ApJ*, 262, 590
- Fujita, S., Torii, K., Tachihara, K., et al. 2019, *ApJ*, 872, 49
- Fujita, S., Torii, K., Kuno, N., et al. 2021a, *PASJ*, 73, S172. doi:10.1093/pasj/psz028
- Fujita, S., Sano, H., Enokiya, R., et al. 2021b, *PASJ*, 73, S201. doi:10.1093/pasj/psaa078
- Fukui, Y., & Kawamura, A. 2010, *ARA&A*, 48, 547
- Fukui, Y., Harada, R., Tokuda, K., et al. 2015, *ApJL*, 807, L4
- Fukui, Y., Torii, K., Ohama, A., et al. 2016, *ApJ*, 820, 26. doi:10.3847/0004-637X/820/1/26
- Fukui, Y., Tokuda, K., Saigo, K., et al. 2019, *ApJ*, 886, 14
- Fukui, Y., Habe, A., Inoue, T., et al. 2021, *PASJ*, 73, S1. doi:10.1093/pasj/psaa103
- Goldreich, P. & Kwan, J. 1974, *ApJ*, 189, 441. doi:10.1086/152821
- Goodman, A. A., Alves, J., Beaumont, C. N., et al. 2014, *ApJ*, 797, 53. doi:10.1088/0004-637X/797/1/53
- Gratier, P., Braine, J., Rodriguez-Fernandez, N. J., et al. 2010, *A&A*, 522, A3. doi:10.1051/0004-6361/201014441
- Griffin, M. J., Abergel, A., Abreu, A., et al. 2010, *A&A*, 518, L3
- Green, D. A. 2019, *Journal of Astrophysics and Astronomy*, 40, 36
- Guetter, H. H. 1992, *AJ*, 103, 197
- Heyer, M., & Dame, T. M. 2015, *ARA&A*, 53, 583
- Habe, A. & Ohta, K. 1992, *PASJ*, 44, 203
- Hasegawa, Y., Asayama, S., Harada, R., et al. 2017, *PASJ*, 69, 91. doi:10.1093/pasj/psx098
- Haworth, T. J., Tasker, E. J., Fukui, Y., et al. 2015, *MNRAS*, 450, 10. doi:10.1093/mnras/stv639
- Higuchi, A. E., Kurono, Y., Saito, M., et al. 2009, *ApJ*, 705, 468
- Higuchi, A. E., Kurono, Y., Saito, M., et al. 2010, *ApJ*, 719, 1813
- Hunter, J. D. 2007, *Computing in Science and Engineering*, 9, 90
- Hasegawa, T., Sato, F., Whiteoak, J. B., et al. 1994, *ApJL*, 429, L77. doi:10.1086/187417
- Inoue, T. & Fukui, Y. 2013, *ApJL*, 774, L31. doi:10.1088/2041-8205/774/2/L31
- Inoue, T., Hennebelle, P., Fukui, Y., et al. 2018, *PASJ*, 70, S53. doi:10.1093/pasj/psx089
- Jackson, J. M., Finn, S. C., Chambers, E. T., et al. 2010, *ApJL*, 719, L185. doi:10.1088/2041-8205/719/2/L185
- Kamazaki, T., Okumura, S. K., Chikada, Y., et al. 2012, *PASJ*, 64, 29
- Kauffmann, J., Bertoldi, F., Bourke, T. L., et al. 2008, *A&A*, 487, 993
- Koda, J., Scoville, N., Sawada, T., et al. 2009, *ApJL*, 700, L132
- Kohn, M., Torii, K., Tachihara, K., et al. 2018, *PASJ*, 70, S50
- Kohn, M., Tachihara, K., Torii, K., et al. 2021a, *PASJ*, 73, S129. doi:10.1093/pasj/psaa015
- Kohn, M., Tachihara, K., Fujita, S., et al. 2021b, *PASJ*, 73, S338. doi:10.1093/pasj/psy109
- Kondo, H., Tokuda, K., Muraoka, K., et al. 2021, *ApJ*, 912, 66. doi:10.3847/1538-4357/abeb65
- Koo, B.-C. 1999, *ApJ*, 518, 760
- Kumar, B., Sagar, R., Sanwal, B. B., et al. 2004, *MNRAS*, 353, 991
- Kumar, M. S. N., Kamath, U. S., & Davis, C. J. 2004, *MNRAS*, 353, 1025
- Kuno, N., et al. 2011, in *Proc. 2011 XXXth URSI General Assembly and Scientific Symposium* (New York: IEEE), 3670⁵
- Kutner, M. L., & Ulich, B. L. 1981, *ApJ*, 250, 341
- Lada, C. J., & Lada, E. A. 2003, *ARA&A*, 41, 57
- Lada, C. J., Bergin, E. A., Alves, J. F., et al. 2003, *ApJ*, 586, 286. doi:10.1086/367610
- Li, G.-X., Wyrowski, F., Menten, K., et al. 2013, *A&A*, 559, A34. doi:10.1051/0004-6361/201322411
- Liu, H.-L., Stutz, A., & Yuan, J.-H. 2019, *MNRAS*, 487, 1259. doi:10.1093/mnras/stz1340
- Lortet-Zuckermann, M. C. 1974, *A&A*, 30, 67
- Marín-Franch, A., Herrero, A., Lenorzer, A., et al. 2009, *A&A*, 502, 559
- Martín-Hernández, N. L., Bik, A., Puga, E., et al. 2008, *A&A*, 489, 229
- Massey, P., Johnson, K. E., & Degioia-Eastwood, K. 1995, *ApJ*, 454, 151
- Matsumoto, T., Dobashi, K., & Shimoikura, T. 2015, *ApJ*, 801, 77. doi:10.1088/0004-637X/801/2/77
- McClure-Griffiths, N. M., & Dickey, J. M. 2016, *ApJ*, 831, 124
- McKee, C. F., & Ostriker, E. C. 2007, *ARA&A*, 45, 565
- Minamidani, T., Umemoto, T., Nishimura, A., et al. 2015, *EAS Publications Series*, 75-76, 193. doi:10.1051/eas/1575036
- Minamidani, T., Nishimura, A., Miyamoto, Y., et al. 2016, *Proc. SPIE*, 9914, 99141Z. doi:10.1117/12.2232137
- Miyamoto, Y., Nakai, N., & Kuno, N. 2014, *PASJ*, 66, 36
- Molinari, S., Swinyard, B., Bally, J., et al. 2010a, *PASP*, 122, 314
- Molinari, S., Swinyard, B., Bally, J., et al. 2010b, *A&A*, 518, L100
- Molinari, S., Schisano, E., Elia, D., et al. 2016, *A&A*, 591, A149
- Morgan, W. W., Whitford, A. E., & Code, A. D. 1953, *ApJ*, 118, 318
- Motte, F., Bontemps, S., & Louvet, F. 2018, *ARA&A*, 56, 41
- Mottram, J. C. & Brunt, C. M. 2012, *MNRAS*, 420, 10. doi:10.1111/j.1365-2966.2011.19843.x
- Nakajima, T., Inoue, H., Fujii, Y., et al. 2019, *PASJ*, 71, S17
- Nakamura, F., Sugitani, K., Tanaka, T., et al. 2014, *ApJL*, 791, L23. doi:10.1088/2041-8205/791/2/L23
- Nakanishi, H., Fujita, S., Tachihara, K., et al. 2020, *PASJ*, 72, 43. doi:10.1093/pasj/psaa027
- Nishimura, A., Tokuda, K., Kimura, K., et al. 2015, *ApJS*, 216, 18
- Nishimura, A., Minamidani, T., Umemoto, T., et al. 2018, *PASJ*, 70, S42
- Nishimura, A., Fujita, S., Kohn, M., et al. 2021, *PASJ*, 73, S285. doi:10.1093/pasj/psaa083

- Nishimura, A., Tokuda, K., Harada, R., et al. 2020, *Proc. SPIE*, 11445, 114457F. doi:10.1117/12.2560955
- Ohashi, N., Hayashi, M., Ho, P. T. P., et al. 1997, *ApJ*, 475, 211. doi:10.1086/303533
- Olm, L., Araya, E. D., Chapin, E. L., et al. 2010, *ApJ*, 715, 1132. doi:10.1088/0004-637X/715/2/1132
- Onishi, T., Nishimura, A., Ota, Y., et al. 2013, *PASJ*, 65, 78
- Perez, F., & Granger, B. E. 2007, *Computing in Science and Engineering*, 9, 21
- Pigulski, A., Kolaczowski, Z., & Kopacki, G. 2000, *ACTAA*, 50, 113
- Pilbratt, G. L., Riedinger, J. R., Passvogel, T., et al. 2010, *A&A*, 518, L1
- Pineda, J. E., Caselli, P., & Goodman, A. A. 2008, *ApJ*, 679, 481
- Pineda, J. L., Goldsmith, P. F., Chapman, N., et al. 2010, *ApJ*, 721, 686
- Pipher, J. L., Sharpless, S., Savedoff, M. P., et al. 1977, *A&A*, 59, 215
- Poglitsch, A., Waelkens, C., Geis, N., et al. 2010, *A&A*, 518, L2
- Priestley, F. D. & Whitworth, A. P. 2021, *MNRAS*, 506, 775. doi:10.1093/mnras/stab1777
- Ragan, S. E., Henning, T., Tackenberg, J., et al. 2014, *A&A*, 568, A73
- Reid, M. J., Dame, T. M., Menten, K. M., et al. 2016, *ApJ*, 823, 77
- Reid, M. J., Menten, K. M., Brunthaler, A., et al. 2019, *ApJ*, 885, 131
- Riaz, B., Martín, E. L., Tata, R., et al. 2012, *MNRAS*, 419, 1887
- Robitaille, T., & Bressert, E. 2012, *APLpy: Astronomical Plotting Library in Python*, ascl:1208.017
- Rodón, J. A., Beuther, H., & Schilke, P. 2012, *A&A*, 545, A51
- Russeil, D., Schneider, N., Anderson, L. D., et al. 2013, *A&A*, 554, A42
- Sagar, R., & Joshi, U. C. 1981, *Ap&SS*, 75, 465
- Saigo, K., Onishi, T., Nayak, O., et al. 2017, *ApJ*, 835, 108
- Saito, H., Saito, M., Sunada, K., et al. 2007, *ApJ*, 659, 459
- Sano, H., Tsuge, K., Tokuda, K., et al. 2021, *PASJ*, 73, S62. doi:10.1093/pasj/psaa045
- Sault, R. J., Teuben, P. J., & Wright, M. C. H. 1995, *Astronomical Data Analysis Software and Systems IV*, 77, 433
- Sawada, T., Ikeda, N., Sunada, K., et al. 2008, *PASJ*, 60, 445
- Sharpless, S. 1959, *ApJS*, 4, 257
- Shi, H. M., & Hu, J. Y. 1999, *A&AS*, 136, 313
- Shimoikura, T., Dobashi, K., Matsumoto, T., et al. 2016, *ApJ*, 832, 205. doi:10.3847/0004-637X/832/2/205
- Shimoikura, T., Dobashi, K., Nakamura, F., et al. 2018, *ApJ*, 855, 45. doi:10.3847/1538-4357/aaaccd
- Sofue, Y., Kohno, M., Torii, K., et al. 2019, *PASJ*, 71, S1. doi:10.1093/pasj/psy094
- Sofue, Y. & Kohno, M. 2020, *MNRAS*, 497, 1851. doi:10.1093/mnras/staa2056
- Stone, R. C. 1988, *AJ*, 96, 1389
- Szymczak, M., Hrynek, G., & Kus, A. J. 2000, *A&AS*, 143, 269. doi:10.1051/aas:2000334
- Takahira, K., Tasker, E. J., & Habe, A. 2014, *ApJ*, 792, 63. doi:10.1088/0004-637X/792/1/63
- Taylor, A. R., Wallace, B. J., & Goss, W. M. 1992, *AJ*, 103, 931
- Tokuda, K., Fukui, Y., Harada, R., et al. 2019, *ApJ*, 886, 15
- Tokuda, K., Muraoka, K., Kondo, H., et al. 2020, *ApJ*, 896, 36
- Torii, K., Enokiya, R., Sano, H., et al. 2011, *ApJ*, 738, 46. doi:10.1088/0004-637X/738/1/46
- Torii, K., Fujita, S., Matsuo, M., et al. 2018, *PASJ*, 70, S51. doi:10.1093/pasj/psy019
- Torii, K., Fujita, S., Nishimura, A., et al. 2019, *PASJ*, 71, S2
- Torii, K., Hattori, Y., Matsuo, M., et al. 2021, *PASJ*, 73, S368. doi:10.1093/pasj/psa098
- Tsuge, K., Fukui, Y., Tachihara, K., et al. 2021, *PASJ*, 73, S35. doi:10.1093/pasj/psaa033
- Tsuge, K., Tachihara, K., Fukui, Y., et al. 2021, *PASJ*, 73, 417. doi:10.1093/pasj/psab008
- Turner, D. G. 1979, *JRASC*, 73, 74
- Turner, D. G. 1986, *A&A*, 167, 157
- Ulich, B. L., & Haas, R. W. 1976, *ApJS*, 30, 247
- Umemoto, T., Minamidani, T., Kuno, N., et al. 2017, *PASJ*, 69, 78
- van der Walt, S., Colbert, S. C., & Varoquaux, G. 2011, *Computing in Science and Engineering*, 13, 22
- VERA Collaboration, Hirota, T., Nagayama, T., et al. 2020, *PASJ*, 72, 50. doi:10.1093/pasj/psaa018
- Wada, K., & Koda, J. 2004, *MNRAS*, 349, 270
- Wang, K., Testi, L., Ginsburg, A., et al. 2015, *MNRAS*, 450, 4043. doi:10.1093/mnras/stv735
- Wang, Y., Beuther, H., Schneider, N., et al. 2020, *A&A*, 641, A53. doi:10.1051/0004-6361/202037928
- Wilson, T. L., & Rood, R. 1994, *ARA&A*, 32, 191
- Wilson, T. L., Rohlfs, K., & Hüttemeister, S. 2013, *Tools of Radio Astronomy; Astronomy and Astrophysics Library*. ISBN 978-3-642-39949-7. Springer-Verlag Berlin Heidelberg
- Wu, B., Van Loo, S., Tan, J. C., et al. 2015, *ApJ*, 811, 56. doi:10.1088/0004-637X/811/1/56
- Xu, J.-W., Zhang, X.-Z., & Han, J.-L. 2005, *CIAA*, 5, 165
- Xu, J.-L., & Wang, J.-J. 2012, *A&A*, 543, A24
- Xu, Y., Reid, M. J., Menten, K. M., et al. 2009, *ApJ*, 693, 413
- Xu, J.-L. & Ju, B.-G. 2014, *A&A*, 569, A36. doi:10.1051/0004-6361/201423952
- Xu, Y., Reid, M., Dame, T., et al. 2016, *Science Advances*, 2, e1600878
- Xu, Y., Bian, S. B., Reid, M. J., et al. 2018, *A&A*, 616, L15
- Xu, Y., Hou, L. G., Bian, S. B., et al. 2021, *A&A*, 645, L8. doi:10.1051/0004-6361/202040103
- Xue, R., & Wu, Y. 2008, *ApJ*, 680, 446
- Yajima, Y., Sorai, K., Miyamoto, Y., et al. 2021, *PASJ*. doi:10.1093/pasj/psaa119
- Yamada, R., Fukui, Y., Sano, H., et al. 2021, *arXiv:2106.01852*
- Yoda, T., Handa, T., Kohno, K., et al. 2010, *PASJ*, 62, 1277
- Zhang, M., Kainulainen, J., Mattern, M., et al. 2019, *A&A*, 622, A52. doi:10.1051/0004-6361/201732400
- Zucker, C., Battersby, C., & Goodman, A. 2015, *ApJ*, 815, 23. doi:10.1088/0004-637X/815/1/23
- Zychová, L. & Ehlerová, S. 2016, *A&A*, 595, A49. doi:10.1051/0004-6361/201527897

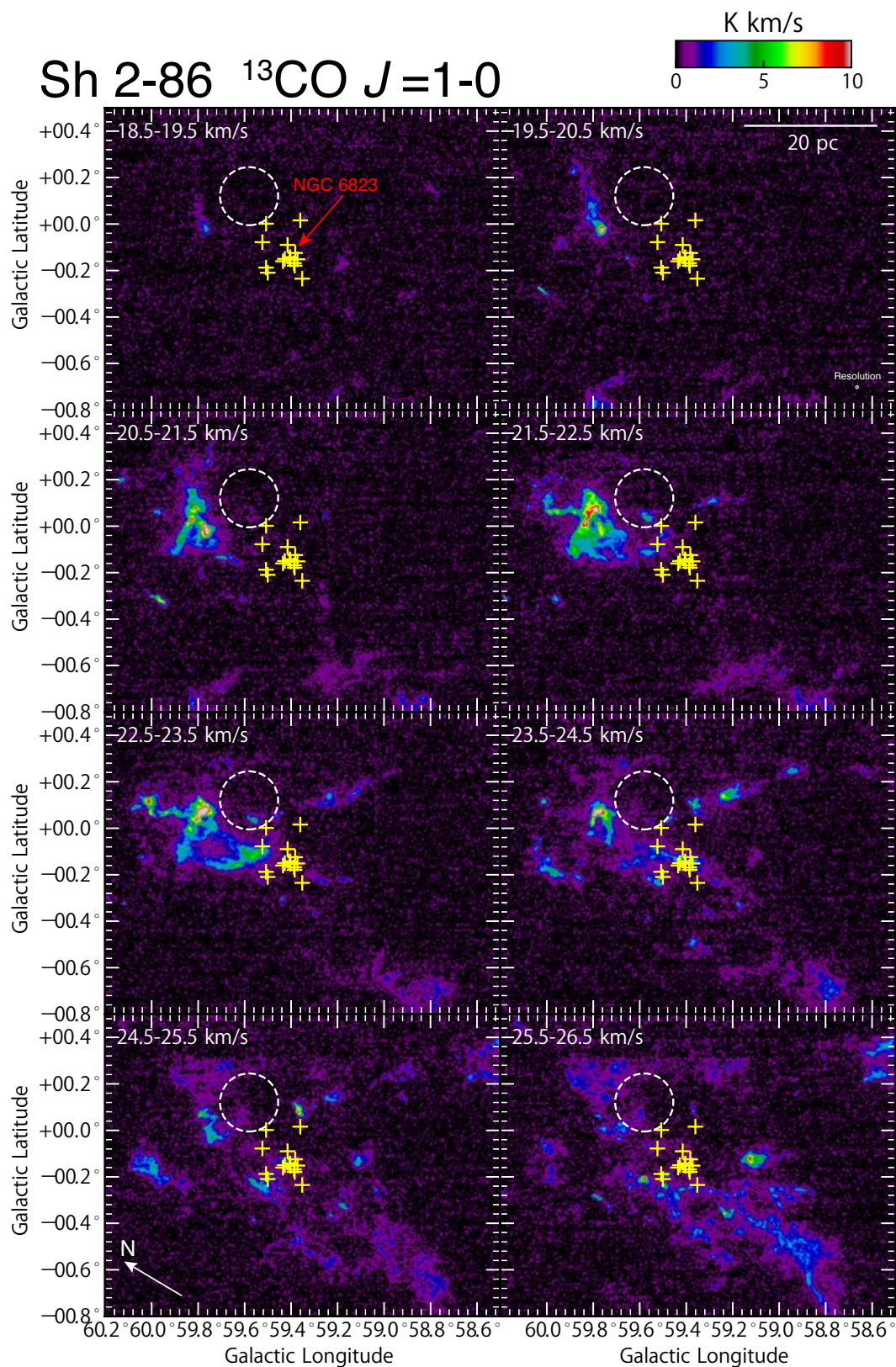


Fig. 11. Velocity-channel map of the $^{13}\text{CO } J=1-0$ emission with a velocity step of 1.0 km s^{-1} . The crosses and dotted circles are the same as in Figure 1(b). The map resolution after convolution is $40''$. The 1σ noise level is $\sim 0.3 \text{ K km s}^{-1}$ for the velocity interval of 1.0 km s^{-1} .

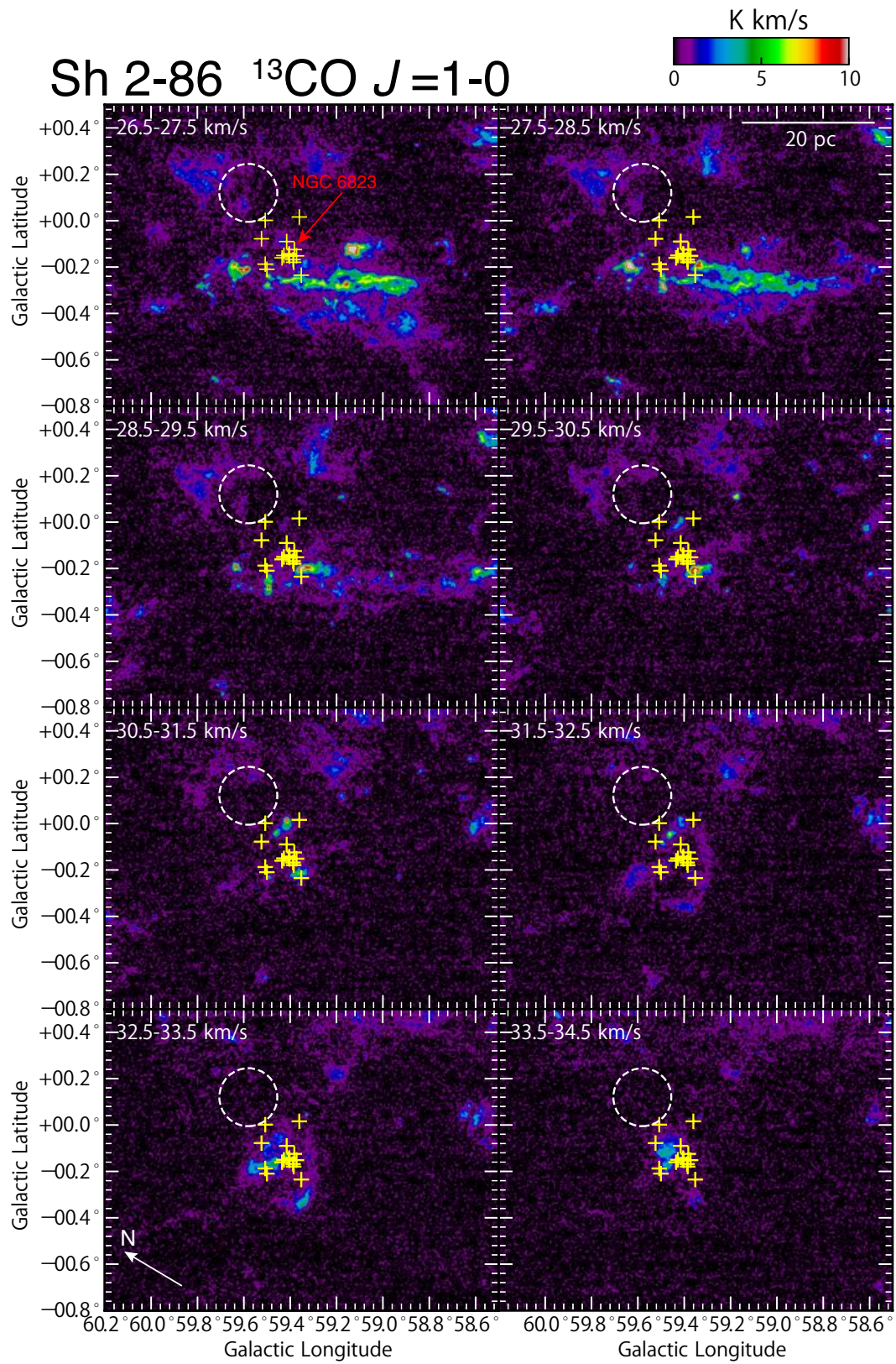
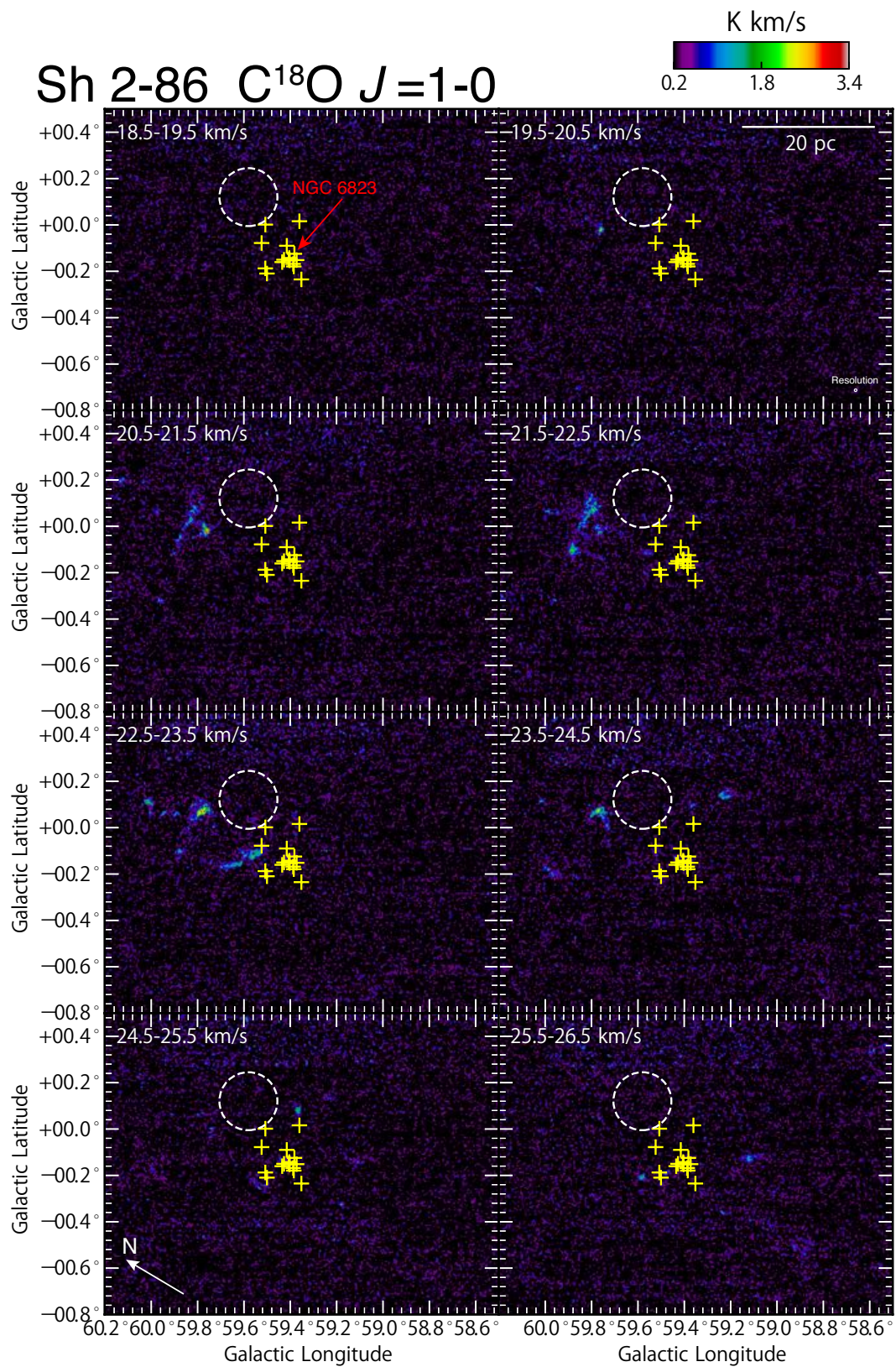


Fig. 11. (Continued.)

Fig. 12. Same as Figure 11, but for C¹⁸O $J=1-0$

